Charles University in Prague
Faculty of Mathematics and Physics

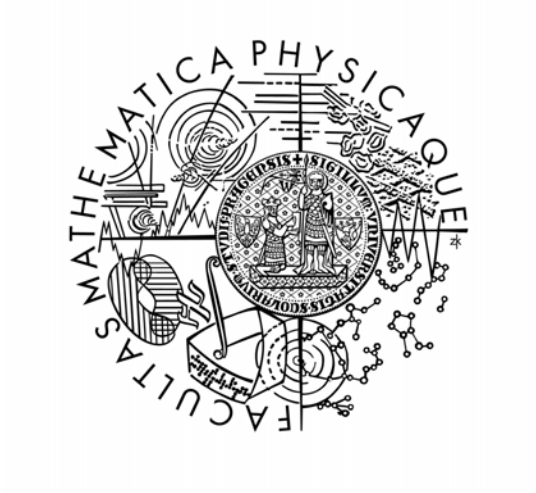

Doctoral thesis

Study of magnetic properties of the $RT^1_{1-x}T^2_xX$ compounds

RNDr. Jiří Prchal

Department of Electronic Structures

Supervisor: Doc. Mgr. Pavel Javorský, Dr.
Consultant: Dr. Karel Prokeš, DrSc.

Prague, September 2006

This thesis would not be possible to arise in the present form without help of many people whom I would like to say my best thanks.

My greatest thanks belong to my supervisor, Doc. Mgr. Pavel Javorský, Dr. His supervising was my big pleasure and he always supported me during all work on my thesis. He helped me at many experiments, I am also thankful to him for helping me to understand the studied problems and for his assistance with any problem anytime I needed, as well as for his discussions and help while formatting this thesis.

I wish to express another big thanks to my adjunct supervisor, Dr. Hideaki Kitazawa, who supervised me during my one-year stay in National Institute for Materials Science in Tsukuba. His everyday care and support made my stay in Japan very fruitful and successful, as well as his assistance in the personal life in Japan helped me to explore this nice country and to discover its habits, which were unknown to me before.

I am also grateful to Prof. RNDr. Vladimír Sechovský, DrSc. for inspiring me into the area of magnetic studies, for his support and care about my work, and also for his personal understanding.

My gratitude belongs to Ing. Josef Šebek, PhD. for introducing me to the magnetic studies seven years ago and for his patience with my work already during my high-school studies.

Another big thank belongs to Dr. Karel Prokeš, DrSc., he taught me a lot about a single-crystal neutron diffraction during my two-months stay in HMI Berlin. I am thankful to him for many useful discussions and patient explanations.

I wish to thank also to Dr. Takashi Naka, who introduced me to high-pressure experiment techniques for his patience during teaching me the new experimental method.

Another thank belongs to Prof. Frank R. de Boer for his help with the high-temperature X-ray diffraction experiment and for his careful reading of my manuscripts.

I would like to thank to Prof. Alexander V. Andreev for many fruitful discussions and introducing me into the field of single-crystals growth. I thank also to Doc. Martin Diviš, CSc. for many patient explanations of theoretical background and help during preparation for oral exams.

My thanks belong to RNDr. Stanislav Daniš, PhD. and Mgr. Zdeněk Matěj for their help with X-ray experiments and discussions concerning the evaluation of the measured data. I am thankful to Ing. Eva Šantavá, CSc. for her care about several of my measurements. I also thank to Doc. RNDr. Pavel Svoboda, CSc. for reading the preliminary versions of this thesis.

I also thank to Mgr. Karel Jurek, CSc. for performance of the microprobe experiment.

I owe thanks to my colleague and friend RNDr. Jan Prokleška, he always helped me with small but painful troubles either on the experimental hardware or on the problems with software on the computer in the office. I express thanks to other colleagues and friends from our department – to RNDr. Jana Poltierová Vejpravová, to RNDr. Ján Rusz, PhD., to Mgr. Khrystyna Miliyanchuk, to Mgr. Klára Uhlířová, to Mgr. Jiří Pospíšil, to Mgr. Matúš Mihálik, to Mgr. Karel Carva and to all other members of our department – for their help in every-day problems and discussions and for friendly atmosphere.

My gratitude belongs to my family, my brothers and especially to my mother, for their interest in my work and support.

I wish to express a special thank to my wife, Markéta, this thesis could not be finished in time without her every-day care and understanding to my work.

Contents

1. Introduction 3

2. Theory 5

2.1 General theory 5
2.2 Scattering of radiation by crystals 11

3. Previous results 15

3.1 *RTX* compounds 15
3.2 *R*NiAl and *R*CuAl 16
3.3 $TbNi_{1-x}Cu_xAl$ 16
3.4 $ErNi_{1-x}Cu_xAl$ 17
3.5 DyNiAl and DyCuAl 19

4. Experimental methods 20

4.1 Sample preparation 20
4.2 X-ray diffraction 22
4.3 Magnetization measurements 23
4.4 Specific heat 24
4.5 Neutron diffraction 24

5. Results 28

5.1 Crystal structure. 28
5.1.1 ZrNiAl-type structure 29
5.1.2 Effect of substitution 30
5.1.3 Temperature evolution 35
5.2 Magnetism 39
5.2.1 $ErNi_{1-x}Cu_xAl$ 40
5.2.2 DyNiAl 44
5.2.3 $DyNi_{1-x}Cu_xAl$ 51

6. Discussion 58

6.1 Crystal structure 58
6.2 Magnetism 61
6.3 Relation between structural and magnetic properties. 63

7. Conclusions 65

8. References 67

1. Introduction

The interest in compounds containing elements with a partly filled electronic *f*-shell has been increasing during the last years because of the physical properties of these materials. In particular, the magnetic behavior caused by the unfilled *f*-shell is being studied. The main difference between 4*f* and 5*f* electrons is that the 4*f* electrons are well localized, whereas the 5*f* electrons exhibit more itinerant behavior.

The ternary compounds exhibit a larger number of different structure types and, on the other hand, they also exhibit a larger number of compounds that crystallize in the same structure type. Therefore, the rare-earth ions can be studied in various types of crystalline environments. When substituting other elements, one may gradually change the number of electrons in the system. Subsequent addition of *d*-electrons to the compound – by substituting the transition-metal atoms by atoms of a neighboring element in the Periodic System – may lead to a change in the type of magnetic ordering which, in rare-earth compounds, is mediated mainly by the electrons in the conduction band.

This work is focused on the structural and, mainly, magnetic behavior of $R\mathrm{Ni}_{1-x}\mathrm{Cu}_x\mathrm{Al}$ pseudo-ternary series with R = Er and Dy, where Cu is being substituted for Ni. These compounds belong to the large group of *RTX* compounds (R ~ rare-earth, T ~ transition metal, X ~ *p*-metal) crystallizing in the hexagonal ZrNiAl-type structure. The motivation to deal just by these series originates from previous studies of the *R*NiAl and *R*CuAl compounds [1,2] at the Department of Electronic Structures of Charles University and from interesting results obtained on similar $\mathrm{TbNi}_{1-x}\mathrm{Cu}_x\mathrm{Al}$ compounds by Ehlers et al. [3]. The present work is also a continuation of previous results of bulk measurements on the Er-based series, performed in the framework of the diploma thesis of the author of the present doctoral thesis [4], which arose further questions about the evolution of magnetic structures and about the nature of the magnetic behavior. It was decided to select Er and Dy as the rare-earth element in the studied compounds in order to compare two examples with either 1) different type of magnetic ordering and moreover different magnetocrystalline anisotropy in the parent compounds (the case of $\mathrm{ErNi}_{1-x}\mathrm{Cu}_x\mathrm{Al}$ series) or 2) similar behavior of both parent compounds in the case of the Dy-based series.

During the present investigation, polycrystalline samples with selected values of the parameter x and a DyNiAl single crystal have been prepared, attested and studied by means of X-ray-diffraction, magnetization, heat-capacity and especially neutron-diffraction experiments to obtain information about the crystal structure, the bulk magnetic properties and the magnetic structures themselves. Based on the

previous discovery of the structural discontinuity in the Er-based series, we have been looking for the connection between the structural step and the magnetic properties. Seeking for common signs of 1) the substitution in the RNi$_{1-x}$Cu$_x$Al series and 2) joint connections between the structural and magnetic evolution in these compounds belonged to the main goals of this work.

This thesis is organized in the following way. The theory necessary to understand the observed effects and also a summary of the theory used in the scattering techniques (neutron and X-ray diffraction) are included in Chapter 2. Theory. Results already known before we started to collect the results for this thesis are included in Chapter 3. Previous results. Section 4. Experimental methods describes the techniques used for sample preparation and collecting the experimental data. Chapter 5. Results represents the main part of the thesis showing all experimental data. These results are discussed in the Chapter 6. Discussion and Chapter 7. Conclusions contains the main results reached.

2. Theory

2.1 General theory

Rare-earth ions

The set of elements positioned between lanthanum (Z = 57) and lutetium (Z = 71) in the Periodic Table of Elements are called 'lanthanides' and together with scandium (Z = 21) and yttrium (Z = 39) from the group called 'Rare earths' (for historical reasons). The elements from lanthanum to europium (Z = 63) are usually indicated as 'light rare-earths' and the others (i.e. Gd to Lu) are 'heavy rare earths'. In the further text we will mark them all as '*R*'. The theory of rare-earth ions is described in the literature – e.g. [5-7], we will focus on several basic aspects of the theory.

It is known, that the atomic radius of rare earths decreases with increasing atomic number. This is the so-called lanthanide-contraction. The electronic configuration of these elements can be generally written as:

$$[\mathrm{Xe}]\ 6s^2 5d^1 4f^N. \qquad (2.1)$$

Just the 4*f* electrons are responsible for the magnetic moments. Thus, the magnetic behavior of the rare-earths originates from the consequent filling of the electronic 4*f*-shell in the *R* series.

Because the energy of 5*d* electrons is higher than that of the 4*f*, the rare-earth atoms are mostly found in the trivalent state (except for Ce, Eu and Yb). In the conducting solids, the 5*d* and 6*s* electrons are delocalized and create the conduction band.

The 4*f* shell has a much (about ten times) smaller radial extent (≈ 40 pm) then the the typical distance between neighboring rare-earth atoms in a solid and is also shielded by the filled 6*s* and 5*p* shells. Therefore, the character of the 4*f* electrons is rather localized, unlike to that of 5*f* electrons in actinides, which exhibit all types of behavior between localized and itinerant. This is why one may consider rare-earth atoms in a solid as free ions in a sea of conduction electrons with *s*, *p* and *d* character. The 4*f* level of such ion is not directly influenced by the neighboring atoms and the states of the 4f electrons depend on their interaction with the charge of nucleus, which is shielded by the inner filled-electron shells, and with other 4*f* electrons. The effect of other filled shells can be included in an effective nuclear charge in the central potential

of an effective charge of $+\widetilde{Z}e$. When neglecting the spin-orbit interaction, the total Hamiltonian of such system is given by

$$\hat{H}_{4f} = \sum_{i=1}^{N}\left(-\frac{\eta^2}{2m_e}\right)\nabla_i^2 + \sum_{i=1}^{N}-\frac{\widetilde{Z}e^2}{\boldsymbol{r}_i} + \sum_{i<j}\frac{e^2}{\boldsymbol{r}_{ij}} . \qquad (2.2)$$

Here, $\hbar$, m_e and e are Planck's constant, the static mass and the charge of an electron, respectively. The variables $\boldsymbol{r}_i$ and $\boldsymbol{r}_{ij}$ are the positions of the electron in relation to the central potential and of the electrons with respect to each other. Since the inter-electronic distances are highly correlated, we can use the Hartree-Fock approximation for classifying the energy levels:

$$\hat{H}_0 = \sum_{i=1}^{N}\left(-\frac{\eta^2}{2m_e}\right)\nabla_i^2 + \sum_{i=1}^{N}-\frac{\widetilde{Z}e^2}{\boldsymbol{r}_i} + \sum_{i=1}^{N}V_i(\boldsymbol{r}) , \qquad (2.3)$$

where $V_i(\boldsymbol{r})$ are the Hartree-Fock self-consistent potentials.

The electron states are characterized by the hydrogen-like wave functions

$$\psi_{nlm_lm_s}(\boldsymbol{r},\sigma) = R_{nl}(r)\cdot Y_{m_l}(\vartheta,\varphi)\cdot\chi_{m_s}(\sigma) , \qquad (2.4)$$

where $R_{nl}(r)$, $Y_{m_l}(\vartheta,\varphi)$ and $\chi_{m_s}(\sigma)$ are the radial, spherical and spin wave functions, respectively, and n, l, m_l, m_s are the basic, orbital, magnetic and spin quantum numbers.

The ground state corresponding to the $4f^N$ electron configuration can be determined by the assignment of N electrons to the $4f$ one-electron states ($n = 4$, $l = 3$). The total wave function can be represented by a Slater determinant of N one-electron wave functions. The ground state is generally degenerate with a degeneracy of $\binom{14}{N}$. This degeneracy is partly removed by the correlation and spin-orbit interactions.

The correlation interaction is given by:

$$\hat{H}_{corr} = \sum_{i<j}\frac{e^2}{r_{ij}} - \sum_{i=1}^{N}V_i(\boldsymbol{r}) . \qquad (2.5)$$

Because the correlation interaction is much smaller than the interaction given by $\hat{H}_0$, it can be computed as a perturbation of the Hamiltonian (2.3). This interaction is the origin of splitting of the states into so-called terms, which are characterized by the orbital ($\boldsymbol{L} = \sum \boldsymbol{l}_i$) and spin moments ($\boldsymbol{S} = \sum \boldsymbol{s}_i$). The operators $\hat{\boldsymbol{L}}^2$, $\hat{\boldsymbol{S}}^2$, $\hat{\boldsymbol{L}}_z$ and $\hat{\boldsymbol{S}}_z$ commute with $\hat{H}_{\text{corr}}$, so the stationary states are given by the values of L, S, M_L and M_S. The energy levels do not depend on M_L and M_S and they stay $(2L+1)(2S+1)$-fold degenerate according to the values of M_L and M_S. The ground term is defined by the following Hund's rules [6]:

1. S reaches a maximum while maintaining the Pauli exclusion principle.
2. L has a maximum value in accordance with the first rule.

The spin-orbit interaction originates from the relativistic correlation between the electron spin and its own orbital moment. In our case (rare-earth intermetallics), it is much weaker than the correlation interaction and can be included as a perturbation. According to the Russel-Saunders approximation, the Hamiltonian of the spin-orbit interaction can be taken as a coupling between $\hat{\boldsymbol{L}}$ and $\hat{\boldsymbol{S}}$:

$$\hat{H}_{\text{LS}} = \lambda(LS) \cdot \hat{\boldsymbol{L}}\hat{\boldsymbol{S}} \ , \qquad (2.6)$$

where λ is the effective spin-orbit constant. This spin-orbit interaction leads to a splitting of the spectral terms into so-called multiplets, according to the total angular momentum $\boldsymbol{J} = \boldsymbol{L}+\boldsymbol{S}$. Each multiplet remains $(2J+1)$-fold degenerate. The ground-state multiplet can be determined from the third Hund's rule: $J = |L - S|$ for the light rare earths for which the 4*f*-shell is filled for less than half ($N < 7$) and $J = L + S$ for the heavy-rare earths ($N \geq 7$). The magnetic moment and the spin of the ground-state multiplet are given by $\boldsymbol{\mu} = -\mu_B g_J \boldsymbol{J}$ and $\boldsymbol{S} = (g_J - 1)\boldsymbol{J}$, where g_J is the Landé factor:

$$g_J = 1 + \frac{J(J+1) + S(S+1) - L(L+1)}{2J(J+1)} \ . \qquad (2.7)$$

The crystal field

In a crystalline environment, the surrounding ions and electrons of the rare-earth ion produce an electric field which acts on the *4f* electrons. This field is called the crystalline electric field, briefly crystal field, and has the symmetry of the

crystal lattice. In the case of the rare earths, the 4*f* moments are rather well shielded by the full 6*s* and 5*d* shells, the "4*f*-electrons — crystal-field" interaction is rather weak and can be considered as a perturbation to $\hat{H}_{LS}$. This perturbation leads to a complete or a partial removal of the degeneracy of the ground-state multiplet.

In first approximation, the crystal-field Hamiltonian $\hat{H}_{CF}$ can be simply computed using the point-charge model. The surrounding electric charges produce an electrostatic potential, which at the position $\boldsymbol{r} = (r, \theta, \varphi)$ can be expressed as:

$$V_{CF}(\boldsymbol{r}) = \sum_j \frac{q_j}{|\boldsymbol{R}_j - \boldsymbol{r}|} , \tag{2.8}$$

where q_j is the charge of an ion at the position $\boldsymbol{R}_j$. If a charge q_i is at $\boldsymbol{r}_i$, then the crystal-field Hamiltonian is given by:

$$\hat{H}_{CF} = \sum_i q_i V_{CF}^i = \sum_{i,j} \frac{q_i q_j}{|\boldsymbol{R}_j - \boldsymbol{r}_i|} , \tag{2.9}$$

where *i* runs over all 4*f* electrons in the unfilled shell.

To determine the energy levels and the eigenfunctions of the rare-earth ion in the crystal field, we have to calculate the matrix elements of the perturbing Hamiltonian between free-ion states. The crystal-field Hamiltonian can be expressed as:

$$\hat{H}_{CF} = \sum_{n,m} B_n^m \hat{O}_n^m . \tag{2.10}$$

Here, B_n^m and $\hat{O}_n^m$ are the crystal-field parameters and the crystal-field operators, respectively [8].

According to the Kramers theorem [9], the energy levels of ions, that have an odd number of electrons (4*f*-electrons for the rare-earths), are at least twofold and evenly degenerate. It has been shown [10] , that ions with an even number of electrons tend to have singlet energy levels in crystals due to the lowered symmetry, that completely removes the degeneracy of the energy levels.

Exchange interactions

Ordering of magnetic moments has its origin in exchange interactions. Generally, in solids there are two basic types of exchange interactions: the direct exchange and the indirect exchange interaction, including the RKKY interaction (see Figure 2.1).

In the Heisenberg model, the exchange-interaction energy between two ions can be expressed as:

$$\hat{H}_{ij\_ex} = -2J_{ij}\hat{\boldsymbol{S}}_i\hat{\boldsymbol{S}}_j \ , \tag{2.11}$$

where J_{ij} is the exchange integral between the spins $\hat{\boldsymbol{S}}_i$ and $\hat{\boldsymbol{S}}_j$. The total Hamiltonian for the whole system is then:

$$\hat{H}_{ex} = -\sum_{\substack{i,j \\ i\neq j}} J_{ij}\hat{\boldsymbol{S}}_i\hat{\boldsymbol{S}}_j \ . \tag{2.12}$$

The direct overlap of the 4*f*-electronic wave functions is negligible in the rare-earth-based compounds. Therefore the direct interaction (typical for 3*d*-metals) usually cannot be considered as responsible for magnetic ordering in these materials. Instead, the indirect interactions should be taken into account.

There are various types of indirect interactions. Here, we mention two of them. The conduction electrons mediate the weak RKKY interaction. These electrons are spin polarized because of the presence of magnetic moments in their surrounding. Owing to properties of conduction electrons, this type of interaction is long range and is oscillating according the distance from the original magnetic ion.

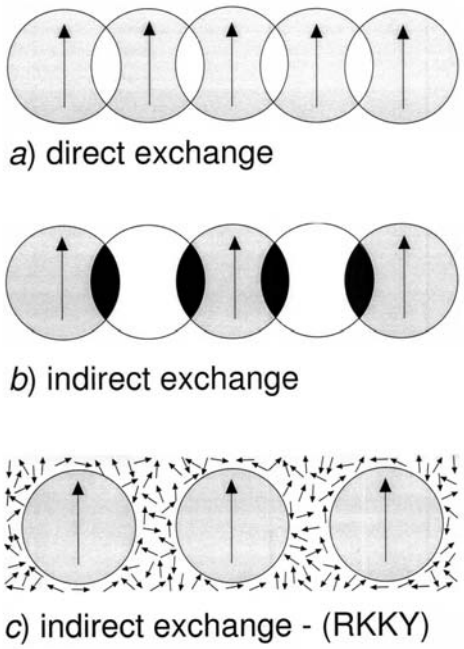

Fig. 2.1: *The basic types of exchange interactions, including the indirect RKKY interaction [5].*

The polarized electrons then interact with the neighboring magnetic moments. This type of interaction is of basic importance in the ordering of magnetic moments of well-localized electrons and is mostly found in lanthanides and their compounds.

For the case of exchange coupling between 4*f*-moments, we mention two mechanisms of indirect exchange. The first one is the RKKY interaction which is mediated by conduction electrons. The Hamiltonian of this interaction is:

$$\hat{H}_{\mathrm{RKKY}} = -\tfrac{1}{2}\sum_{i,j} \mathrm{J}(\boldsymbol{R}_i\text{-}\boldsymbol{R}_j)\boldsymbol{J}_i\boldsymbol{J}_j \ , \qquad (2.13)$$

where we sum over all rare-earth ions with the moment $\boldsymbol{J}_i$. $\mathrm{J}(\boldsymbol{R}_i\text{-}\boldsymbol{R}_j)$ is the effective exchange parameter. The corresponding magnetic-ordering temperature T_C and the paramagnetic Curie temperature θ_p are proportional to the De-Gennes factor $(g_\mathrm{J}\text{-}1)^2 J(J\text{+}1)$.

The second description has been proposed by Campbell [11]. It supposes the coupling between 4*f*-moments to be mediated by the 5*d* rare-earth electrons. As a consequence of the *f*-*d* exchange coupling, a positive local *d*-moment is induced. Because the 5*d* electrons of the rare earth are more delocalized and the wave functions can overlap, one can consider direct exchange interaction, which favors in this case ferromagnetic coupling, and a positive value of the paramagnetic Curie temperature is expected. Furthermore, in compounds with transition metals, the exchange between rare-earth 5*d*-states and *d*-states of the transition metal has to be considered.

2.2 Scattering of radiation by crystals

Scattering techniques are very powerful tool for microscopic study of solids. The radiation used in such experiments can be beams of X-rays, neutrons or electrons. There are generally two different ways in which radiation may be scattered by the crystal lattice: in elastic (diffraction) and in an inelastic way. Since we have used elastic scattering only, we will just describe the background of the diffraction techniques. We have used two of above mentioned probes – X-rays and neutrons – and will briefly describe these two tools.

When interacting with the matter, the wave of the incident radiation scatters at atoms in periodic sets of planes and the scattered waves superpose coherently, resulting in diffracted intensities of the beam distributed in specific directions due to constructive interference.

For a given crystal structure, the positions of the nuclear reflections are given by Bragg's law:

$$\lambda = 2d_{hkl}\sin\theta, \tag{2.14}$$

where λ is the wavelength of the radiation, d_{hkl} is the spacing between the reflecting planes and θ is the angle between the normal to the *hkl*–plane and the direction of interacting radiation.

The intensities of the reflected beam are proportional to the square of the structure factor F_{hkl}:

$$I \approx |F_{hkl}|^2 , \tag{2.15}$$

where F_{hkl} is for the X-ray beam given by

$$F_{hkl} = \sum_i f_{at}(\boldsymbol{q}) \cdot \mathrm{e}^{-2\pi i \boldsymbol{q}\boldsymbol{r}_i} \cdot \mathrm{e}^{-W_i} . \tag{2.16}$$

Here, the summation is over the primitive cell. The parameter $f_{at}(\boldsymbol{q})$ is the atomic dispersion factor. It is the Fourier transform of the electronic charge density $\rho(\boldsymbol{r})$ and is equal to

$$f_{at}(\boldsymbol{q}) = \int_V \rho(\boldsymbol{r}) \mathrm{e}^{i\boldsymbol{q}\boldsymbol{r}} d\boldsymbol{r} . \tag{2.17}$$

The parameter $\boldsymbol{q}$ is the vector in reciprocal space. The expression exp(-W_i) is the temperature factor (square root of the Debye-Waller factor). W_i involves the mean square displacement of the atom around its equilibrium position.

In case of the neutron radiation as incident beam, the atomic dispersion factor f_{at} is replaced by the bound coherent scattering length b_c:

$$F_{hkl} = \sum_i b_c \cdot e^{-2\pi i \boldsymbol{q} \boldsymbol{r}_i} \cdot e^{-W_i}. \tag{2.18}$$

Since the f_{at} is a function of the charge density, the structure factor in the case of X-rays is a monotonous function of the atomic number Z. On the other hand, in the neutron case the parameter b_c is random with respect to the specific element and it can moreover vary within different isotopes (nuclear number A) of a given element. The scattering lengths can be found in the literature – e.g. [12].

The advantage of using a neutron beam for studies of materials is the fact that the neutron has its own spin. The neutrons therefore interact also with the magnetic moments in the matter and interaction with the moments forming a magnetic structure in a material leads to additional diffraction patterns, similar to the ones obtained by diffraction on a periodic crystal structure. The magnetic structure factor F_M is given by

$$\boldsymbol{F}_M = p \sum_j f_j(\boldsymbol{q}) \cdot \boldsymbol{m}_j \cdot e^{i\boldsymbol{q}\boldsymbol{r}} \cdot e^{-W_i}, \tag{2.19}$$

where the sum is over all the magnetic moments within the unit cell. The constant p is equal to $p = \gamma e^2/2m_e c^2 = 0.2696 \cdot 10^{-12}$cm, $f_j(\boldsymbol{q})$ is the magnetic form factor of atom j and $\boldsymbol{m}_j$ is the magnetic moment. The form factors are known for the magnetic moments of the R ions and transition metals [13], but it is often subject of study in uranium compounds with unknkown ratio of spin and orbital moment. The $f_j(\boldsymbol{q})$ function decreases with increasing $\boldsymbol{q}$ (and thus with the scattering angle), similar to $f_{at}(\boldsymbol{q})$ for the X-ray diffraction. In contrast, the scattering lengths b_c is $\boldsymbol{q}$-independent.

Thus, the neutrons interact with the system of nuclei (wave scattering on a particle) and also with the magnetic moments (spin-spin interaction) of the atom. The diffracted intensity of the magnetic scattering is usually of the same order as the intensity from the nuclear diffraction, so that thus we can observe the both – the crystalline (nuclear) and the magnetic structure of a material using the same probe.

Correction of diffracted intensities

The diffracted intensities as measured in the real experiment depend on several factors. A more accurate expression of relation (2.15) is as follows:

$$I_{hkl} = \left(\lambda^3 \frac{V}{V_c^2}\right)\left(\frac{1}{\omega}\right) \cdot L \cdot A \cdot T \cdot E \cdot |F_{hkl}|^2 \quad \text{(neutrons)}, \tag{2.20a}$$

$$I_{hkl} = \left(\lambda^3 r_0^2 \frac{V}{V_c^2}\right)\left(\frac{1}{\omega}\right) \cdot L \cdot P \cdot A \cdot T \cdot E \cdot |F_{hkl}|^2 \quad \text{(X-rays)}, \tag{2.20b}$$

where r_0 is the classical electron radius (e^2/mc^2), V the crystal volume, V_c the unit-cell volume, ω the angular scanning velocity, L the Lorentz factor which is related to the time-of-reflection opportunity, P the polarization factor, A the absorption factor, T the correction for inelastic phonon or thermal-diffuse scattering, and E the correction for extinction and multiple diffraction. After measurement of the diffraction peaks, their intensities should be corrected for the above-mentioned factors. The topicality of these corrections is dependent on the experimental setup and shape and composition of the used sample. For a polycrystalline sample measurement (powder-diffraction experiment), most of these corrections are included already in the programs for the refinement of the measured pattern (e.g. program FullProf [14]) and are described in detail in literature [15-17]. FullProf is one of the programs that allow us to obtain parameters of crystal and/or magnetic structure from measured diffracted intensities or from the whole diffraction profile (in case of powder diffraction). Since we used this particular software in our data evaluation, we will discuss the refinement of the structure using this program. The program FullProf was originally developed for the fitting of the measured patterns from the neutron and X-ray powder diffraction experiments, but nowadays it is able to refine also single-crystal diffraction data. For the refinement, it uses the Rietveld method [18] that is based on initial knowledge of the structure type. By varying the requested (fitted) parameters the method finds the best agreement of the calculated profile wit the measured one.

In case of measurement on a single-crystalline sample, one should consider several of these corrections to be made manually. The exact corrections to be made on the as-measured intensities depend on the used refinement program. In the FullProf program the intensities are listed in a special file as-measured without information about the sample and the arrangement. We will deal a bit more with the two most important corrections that we needed to deal with during refinement.

The correction for the Lorentz factor in our special case of single-crystal diffraction in the equatorial plane should be taken into account in reduced form as

$$L^{-1} = \sin\gamma \cos\nu \,, \qquad (2.21a)$$

where γ is the angle between the incident beam and the projection of the diffracted beam onto the equatorial plane (the plane given by the plane of the movement of the detector), and ν is the angle of the diffracted beam with the equatorial plane. For reflections within the equatorial plane, this expression reduces to

$$L^{-1} = \sin 2\theta \,. \qquad (2.21b)$$

For diffraction made on a powder sample, the Lorentz factor equals:

$$L^{-1} = \sin 2\theta \sin\theta \,. \qquad (2.21c)$$

The intensity of radiation, when passing through matter of thickness t, is reduced according to

$$I = I_0 \, e^{-\mu t} \,, \qquad (2.22a)$$

where μ is the total linear absorption coefficient, and I and I_0 are the transmitted and initial intensities, respectively. If the sample is bathed entirely in the beam (i.e. t being the total path length of the incident and diffracted beams within the crystal for each volume element), the absorption for the whole crystal is obtained by integration over all volume elements, defining the absorption factor A:

$$I = I_0 \frac{1}{V} \int_V e^{-\mu t} dV = I_0 A \,. \qquad (2.22b)$$

It is observed that the mass absorption coefficient μ/ρ, where ρ is the density of the absorber, is reasonable approximation. The value of this expression is independent of the physical state of the absorber and for a compound it is additive to μ/ρ of the elements. Tables of μ/ρ for X-rays are listed in [19], and the values of the absorption cross-sections required to calculate the μ/ρ for neutron experiments are listed in [12].

3. Previous results

3.1 RTX compounds

The *RTX* compounds form a relatively large group of compounds consisted from rare-earth (*R*), transition metal (*T*) and *p*-metal (metal with unfilled *p*-shell of electrons, from the IIIB, IVB or VB group of the Periodic Table) (*X*) elements.

The *RTX* compounds crystallize in various structures. The most usual are three types: orthorhombic TiNiSi-type structure, hexagonal AlB_2-type structure and hexagonal ZrNiAl-type structure.

Most compounds from the *R*NiAl, *R*CuAl, *R*PdAl, *R*NiIn, *R*CuIn, *R*PdIn, *R*AuIn, *R*RhSn and *R*PdTl series crystallize in the ZrNiAl-type hexagonal structure [20]. Generally, in this crystal structure type crystallize more heavy- than light rare-earth based compounds. There are several *RTX* compounds (e.g. TbPtSn [21], TbPdAl [22]), crystallizing in the ZrNiAl-type or in the orthorhombic TiNiSi-type structure, depending on the way of preparation.

From the point of view of magnetic properties, the *RTX* compounds crystallizing in the ZrNiAl-type structure have not been studied so systematically (except for Ce-based compounds) and the interest on these compounds is increasing. Quite complex study on the basis of magnetization, susceptibility, specific heat, electrical resistivity and also neutron diffraction, was performed for the *R*NiAl and *R*CuAl series [1,2] (see below). Just several of the other *RTX* compounds have been studied. An antiferromagnetic (AF) behavior was observed e.g. for some *R*RhSn [23], *R*PtSn [24], *R*AgGe [25,26] compounds. For some of e.g. *R*PtIn [27], *R*PdAl [28] and for DyAgGe [25] ferromagnetic (F) behavior has been reported.

Some anomalous magnetic behavior has been observed for Ce- and Yb-based compounds. For instance CePdIn [29], CePdAl [30-33] and YbNiAl [34,35] were found to be antiferromagnetically ordered with heavy-fermion behavior, CePtIn is a nonmagnetic heavy-fermion system [36], CeNiIn is a valence-fluctuating system with a Kondo-like behavior [37].

The magnetocaloric effect in *RTX* compounds is recently also investigated. The effect itself is not huge in these materials but the correlation between magnetism and magnetocaloric effect attracts attention [38-40].

3.2 RNiAl and RCuAl

Crystal structure of the *R*NiAl and *R*CuAl compounds was first described by Dwight et al. in 1968 [41]. Except for the La-based materials, all the *R*NiAl and *R*CuAl compounds crystallize in the ZrNiAl-type hexagonal structure (space group $P\bar{6}2m$, see chapter 5.1.1 Results – Crystal structure).

In early seventies of the twentieth century there were made deductions about all of these compounds to be subtle ferromagnets, except for CeNiAl, which remains paramagnetic down to the temperature of 4.2 K and for ErNiAl and TmNiAl that were found to behave metamagnetically [42].

Later, in 1992, another results of the magnetic properties of *R*NiAl compounds were published [1,43]. The new measurements showed the compounds with heavy rare-earths (i.e. Gd-Tm) to undergo two or three magnetic phase transitions. Compounds with R = Gd, Tb, Dy, Ho show coexistence of ferro- and antiferromagnetic interactions. The magnetic ordering temperature in the *R*NiAl series is roughly proportional to de-Gennes factor. The exception is PrNiAl where enhanced ordering temperature was ascribed to a stronger hybridization between 4*f* and ligand states. An intermediate valence state of Ce-ions was speculated in CeNiAl. The coexistence of ferromagnetic and antiferromagnetic ordering in *R*NiAl for R = Tb, Dy and Ho has been later confirmed by neutron diffraction experiments [44,45]. Incommensurate magnetic structures have been found in PrNiAl, NdNiAl [46] and YbNiAl [47].

The study of magnetic properties in *R*CuAl series is given in Refs. [2,48]. YCuAl and LuCuAl exhibit a Pauli paramagnetic behavior. The heavy rare-earth *R*CuAl compounds have been found as ferromagnets except for indications of antiferromagnetic ordering observed in low-temperature phase of DyCuAl. No magnetic ordering in TmCuAl was reported in [48], while an AF order below 1.9K was reported in [49]. Complex AF order at low temperatures was finally confirmed by neutron diffraction [50]. Among the light rare-earths, PrCuAl behaves antiferromagnetically and coexistence of ferro- and antiferromagnetic ordering has been observed in NdCuAl [51].

3.3 $TbNi_{1-x}Cu_xAl$

The $TbNi_{1-x}Cu_xAl$ pseudo-ternary compounds were studied by Ehlers et al. [3]. These compounds crystallize in the ZrNiAl-type hexagonal structure within the whole

concentration range of x [3,41]. The parent compounds (TbNiAl; TbCuAl) behave in accordance with the general properties in *R*NiAl and *R*CuAl as described above.

The TbNiAl orders antiferromagnetically below the Néel temperature $T_N = 47$ K, with all Tb moments ordered. One third of Tb moments have considerably reduced magnitude compared to the remaining 2/3 of Tb moments [52]. The compound undergoes another magnetic transition at $T_1 = 23$ K, which is connected with the change of propagation of the frustrated spins. All the Tb moments are of equal size of 8.1 μ_B at 2 K. On the other hand, TbCuAl is a simple ferromagnet with Tb moments along the *c*-axis with the magnitude of 7.7 μ_B [52]. All the Tb moments are of equal value at 2 K.

While increasing the concentration parameter x the lattice constants a and c raise systematically without any unexpected change at 60 K [3]. The ordering temperature changes strongly with the Cu-concentration in the range from 25 K to 59 K over the whole series $TbNi_{1-x}Cu_xAl$. The Curie-Weiss temperature θ_p is positive for both the ferro- and antiferromagnetic compounds. In the range of $0.01 \leq x \leq 0.10$ the coexistence of ferro- and antiferromagnetic ordering was observed. This coexistence is not based on the idea of different parts of the sample with different type of alignment, but there should be "domains" in the whole compound which differ in the type of magnetic order (in the sense of volume with uniform type of order; not Weiss domains). Ferromagnetism has been found above the concentration of $x \geq 0.15$. The exception range of $0.60 \leq x \leq 0.80$ was marked as regime with a dominant short-range magnetic order. A change of the magnetic coupling mediated by *d* electrons (Ni-rich part) to that one mediated mainly by *s* electrons (Cu-rich part) is proposed to explain observed data.

The antiferromagnetic order in TbNiAl is fast suppressed also by substitution of few percent Tb by Y resulting in ferromagnetic order, similar to $TbNi_{1-x}Cu_xAl$ system [53].

3.4 $ErNi_{1-x}Cu_xAl$

In case of the Er-based pseudoternary series the change from an antiferromagnetic triangular-like arrangement within the basal plane, as displayed on Figure 3.1 [54], to a simple ferromagnetic order of magnetic moments

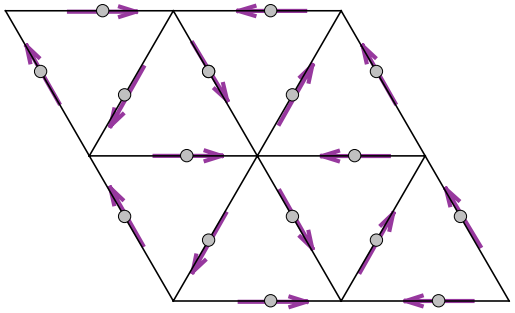

Figure 3.1: Arrangement of the magnetic moments within the *a,b*-plane in the ErNiAl compound [54].

along the *c*-axis was expected. There are two specific changes in this series from the Ni- to the Cu-containing compound. One is change of rhe character of magnetic order

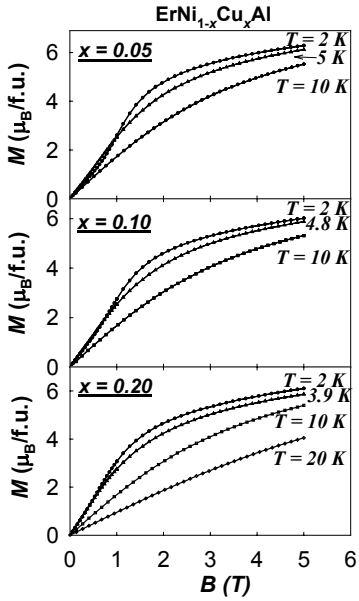

Figure 3.2: Magnetization curves of several $ErNi_{1-x}Cu_xAl$ samples as presented in Ref. [4].

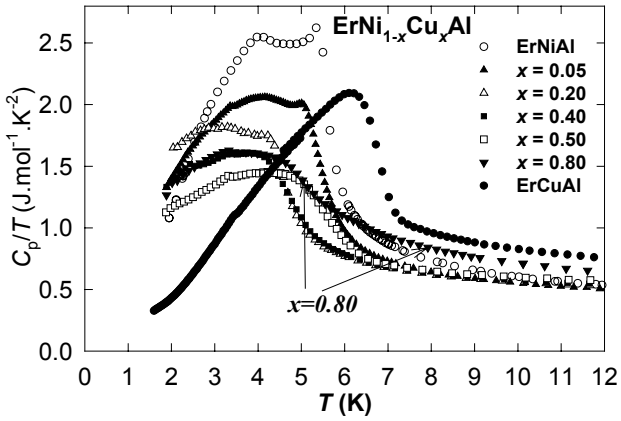

Figure 3.3: Low-temperature part of the heat capacity in the $ErNi_{1-x}Cu_xAl$ series. The figure is taken from [4].

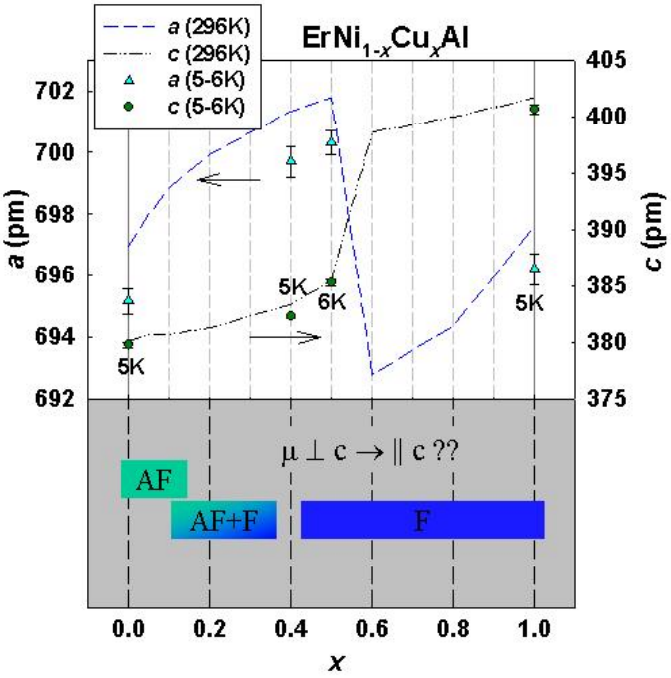

Figure 3.4: The summary of previous results obtained on the $ErNi_{1-x}Cu_xAl$ series – from both structural and magnetic point of view as concluded in [4].

(antiferro- to ferromagnetic) and another is reorientation of the magnetic moments from the hexagonal *a,b*-plane to the direction parallel to crystallographic *c*-axis. Since there was observed a step in the concentration dependence of lattice parameters between $x = 0.5$ and 0.6 at the room temperature (and the suggestion that this step is hold down to at least 5 K was later confirmed), there was a suggestion that this reorientation might be connected with this structural step.

Moreover, the bulk measurements performed on samples from this system showed that character of the studied compounds is consequently changing from antiferromagnetic (for samples with $x \leq 0.2$) to ferromagnetic. The samples with $x \leq 0.2$ exhibit signs of both – ferro- and antiferromagnetic – behavior while the

ferromagnetic one is getting stronger with increasing Cu-content (see Figure 3.2 [4]). The short-range order was not observed on any of the $ErNi_{1-x}Cu_xAl$ samples on the bulk data like it was expected after results from the Tb-based series. The sample with the critical Cu-concentration $x = 0.8$ exhibits ferromagnetic-like behavior similar to parent ErCuAl – that was previously confirmed to be ferromagnetically ordered [54] – just the heat capacity data showed a broader anomaly at potential ordering temperature than the other compounds (Figure 3.3 [55]). Another question arisen after completing the bulk measurements concerned the coexistence of ferromagnetic and antiferromagnetic character in the $x \leq 0.2$ compounds. Summary of these results connected with the structural results are displayed on the Figure 3.4. The unclearnesses about magnetic structures needed to be clarified by the neutron-diffraction experiment.

3.5 DyNiAl and DyCuAl

The DyNiAl compound was studied previously using neutron diffraction on a polycrystalline samples [44,45]. It orders ferromagnetically below $T_C = 31$ K and undergoes another transition at $T_1 = 15$ K where an additional antiferromagnetic component appears. Several discrepancies between results obtained by these two authors needed to be decided, especially the magnitude of the Dy-moments, orientation of the antiferromagnetic component and possible frustration of one third of the Dy moments.

The bulk magnetic properties of DyCuAl were found to be very similar to DyNiAl, thus similar magnetic structure was expected [48]. The magnetic ordering temperatures were found to be also close to DyNiAl – DyCuAl orders at $T_C = 28$ K and another phase-to-phase transition was found at $T_1 = 12$ K. The neutron diffraction experiment was nevertheless not performed on this compound.

4. Experimental methods

4.1 Sample preparation

The polycrystalline samples were prepared by arc-melting in mono-arc furnace either at the Department of Electronic Structures (DES) in Prague or at the National Institute for Materials Science (NIMS) in Tsukuba. In both cases, the preparation was done under protective argon atmosphere – at a pressure of 50 kPa after a previous vacuum of 0.5-2 Pa at DES and – at pressure of ca 90 kPa after previous vacuum of 10^{-3}Pa in case of preparation at NIMS. The polycrystalline samples were turned and remelted five times to achieve better homogeneity.

A single crystal of DyNiAl was grown by using the modified Czochralski method in the tri-arc furnace installed at DES. The amount of initial mixture of the pure elements was about 7g. The alloy was turned several times and then kept in the molten state for about 1 hour to ensure good homogeneity. The single crystal was grown using a tungsten rod as a seed with a pulling speed of 8 mm/hour. Since preparation of the single-crystalline samples of the *RT*Al compounds, especially the *R*CuAl ones (including the substituted series), is very difficult because these are incongruent alloys, we were not able to prepare more samples in the single-crystalline form, although we were trying it several times.

The initial mixture of pure elements, corresponding to the stoichiometric composition of the samples to be prepared, consisted of pure elements with purity of 99.9% for the rare-earth elements (Er, Tb, Dy), 99.995% for Ni and Pd and 99.999% for Cu and Al. In most cases, there a small excess amount of Al was used (0.5 to 1% was added to the expected weight) of Al in order to compensate for evaporation during the melting.

Several samples were wrapped into Ta foil and annealed for 10 days at 900 K. However, as X-ray and microprobe analysis showed, annealing had no effect on the sample quality.

Microprobe

The microprobe analysis of selected samples has been performed at the Institute of Physics, Czech Academy of Sciences, using microanalyser JXA-733 (JEOL). The following lines have been selected for the analysis of individual elements: Al-K_α, Cu-K_α, Er-K_α, Dy-K_α, Ni-L_α. The energy of the electron beam was 20keV. Pure Er, Cu, Al and Ni were used as standards. The weight concentrations

have been obtained from the measured relative intensities (i.e. ratios to the standards) using a ZAF method [56] and a KEVEX program support [57].

The overall view of the surface of the samples has been obtained using COMPO-method. It uses the reverse-scattered electrons whose count is proportional to the mean atomic number of the emitting area. This method is usually being used for resolution of the phases (hence COMPOsition).

The electron-microprobe experiment was performed on selected samples of the Er- and the Dy-based series as well as the DyNiAl single crystal sample. The results of the sample composition of the $ErNi_{1-x}Cu_xAl$ are included in the previous work [55]. The results for selected compounds from the $DyNi_{1-x}Cu_xAl$ series ($x = 0.2$, 0.4, 0.6, 0.8) are shown in the Table 4.1 and the Figure 4.1 displays the microscopic view of one of the samples. The stoichiometric composition of the main phase is in agreement with expected values – it is close (within the error of the method ~ 2-3 %) to the ratio of $R:T:X = 1/3:1/3:1/3$ composition (resulting in 1:1:1 stoichiometry). The ratio of the Ni and Cu content determines the real substitution parameter x. One can see that the real Cu-content is slightly lower in comparison to the nominal one. Nevertheless, this shift is in range of few % what is similar to the accuracy of the experiment itself. Moreover, in all the samples, one minority phase could be visible. This impurity phase corresponds to a stoichiometry approx. $Dy_2T_{4.5}Al_{3.5}$. Such compounds correspond to that ones discovered among the Er-Cu-Al systems [58], corresponding to the category of the $ErCu_{4.2\text{-}2.3}Al_{0.9\text{-}2.7}$ stoichiometry. The impurity phase was observed also in previously studied compounds but no observable influence on the magnetic properties was observed as it was shown by the neutron diffraction and bulk experiments [2,48,54,55].

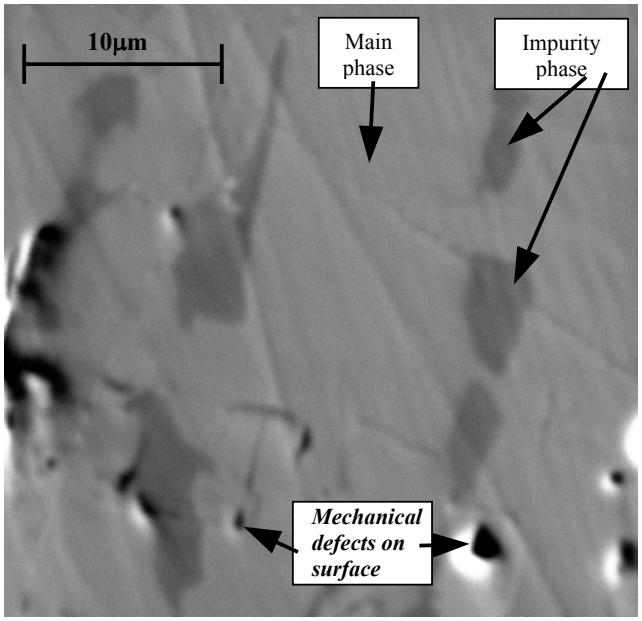

Figure 4.1: Photographic zoom of the surface of the $DyNi_{0.4}Cu_{0.6}Al$ sample studied by the electron-microprobe experiment.

The electron-microprobe experiment performed on the DyNiAl single crystalline sample that was used for the further studies, confirmed a single-phase compound with the real composition of $Dy_{1.05}Ni_{0.98}Al_{0.97}$. The sample was also checked for the phase purity by the X-ray diffraction including determination of the

lattice parameters. The X-ray diffraction pattern was found as a single-phase and the determined lattice parameters were found to be a = 699.8 pm and c = 384.7 pm what is in good agreement with literature data [44,45].

Table 4.1: The composition of the selected $DyNi_{1-x}Cu_xAl$ compounds studied by the electron-microprobe experiment.

		Atomic fraction (in %)				
x	**Phase type**	**Dy**	**Ni**	**Cu**	**Al**	**Real *x***
0.2	**Main phase**	33.87	26.59	5.55	33.99	0.173
	Impurity phase	25.23	28.28	11.12	35.38	
0.4	**Main phase**	34.06	19.76	12.23	33.95	0.382
	Impurity phase	20.73	16.29	29.61	33.36	
0.6	**Main phase**	34.07	13.72	18.06	34.15	0.568
	Impurity phase	18.41	12.00	33.81	35.79	
0.8	**Main phase**	34.26	7.23	22.50	36.01	0.757
	Impurity phase	17.95	5.09	43.56	33.39	

4.2 X-ray diffraction

Room-temperature X-ray diffraction

The X-ray diffraction experiment was used for two purposes – to check the sample quality and also for the study of the crystal structure. All of the samples have been analysed by X-ray powder diffraction at the room temperature with a conventional diffractometer working with the Bragg-Bretano geometry – either Siemens, installed at the DES (Charles University) or Rigaku Rotaflex, installed at NIMS (Tsukuba).

Radiation of Cu (Co) with the wavelengths $\lambda(K\alpha_1)$ = 1.5405 Å and $\lambda(K\alpha_2)$ = 1.5445 Å ($\lambda(K\alpha_1)$ = 1.7889 Å, $\lambda(K\alpha_2)$ = 1.7928 Å, respectively) was used for the experiment. Diffraction patterns were measured with angular resolution of 0.05° (Siemens) or 0.02° (Rigaku).

The data were analysed by the FullProf program [14], which enables to refine data from X-ray and neutron scattering. The structural parameters are refined from the positions and intensities of the observed peaks.

The Laue back-scattering patterns were used to check the single-crystalline state of the DyNiAl and to orient the crystal before cutting the samples.

Low-temperature X-ray diffraction

The study of samples investigated by X-ray diffraction at low temperatures was performed by the method as described above, moreover the cooling option was provided either by a closed-cycle refrigerator (DAIKIN) operating in the temperature range of 8-320K (Rigaku-Rotaflex, NIMS), or the samples were cooled using the He gas as the cooling medium for study in the temperature range from 3.7 K up to 296 K (Siemens, DES). Cu-$K_{\alpha 1,2}$ radiation was used as the incident probe.

High-temperature X-ray diffraction

High-temperature X-ray diffraction was performed on several samples using equipment installed at the Van der Waals-Zeeman Institute of the University of Amsterdam. The instrument consists of a Nonius powder diffractometer with a 120-degrees position-sensitive (bended) Inel detector and electronics. The high-temperature attachment and controller have been purchased from Anton Paar. The heating option was provided by a Pt strip which was the heater element and on which also the powder sample was put. The temperature was measured by means of a Pt-PtRh thermocouple, pointwelded to the bottom of the Pt strip. Measurements were performed under vacuum of about 10^{-6} mbar from room temperature up to 900 °C. Cu-$K_{\alpha 1,2}$ radiation was used and the patterns were measured with a resolution of 0.03°.

4.3 Magnetization measurements

The samples for DC-magnetization measurements were made as powder samples consisting of randomly oriented grains fixed by nonmagnetic glue in a small ampoule. The mass of powder sample was approximately 30-50mg. In the case of the DyNiAl single crystal the sample was fixed by the Teflon holder in the requested orientation with respect to the direction of the external magnetic field.

All the low-temperature and some high-temperature dependencies of DC-magnetization, and all the magnetization curves have been measured at the Joint Laboratory of the Charles University and the Institute of Physics using the Physical Property Measurement System (PPMS) instrument, Quantum Design. Here, the magnetized sample is moved through the detection coils and induces a voltage in the detection coils set. The amplitude of this signal is proportional to the magnetic moment and the speed of the sample during extraction. We have performed

our measurements in the temperature region from 2 to 300 K, in external magnetic fields up to 14 T.

4.4 Specific heat

The specific heat experiments were performed using the PPMS instrument. Measurements were done on polycrystalline samples with the weight of 20-30 mg. The sample was attached to the sample holder by the Apiezon N grease to improve the thermal contact between the sample and the sample holder. The PPMS software uses the two-τ relaxation method to determine the heat capacity values. After reaching high vacuum in the sample space, the required temperature is stabilised and a known pulse is applied. From the time evolution of the temperature one can determine the heat capacity of the system sample holder + Apiezon + sample [59]. If we firstly measure the empty sample holder with the Apiezon, we can determine the heat capacity of the sample itself from the difference between the empty holder and the system sample + holder. The advantage of this method in comparison with classical adiabatic method is a possibility of using small samples that is useful in case of studies of intermetallic samples that cannot be prepared in large amounts (for more details see [59]).

4.5 Neutron diffraction

The magnetic structures (besides the nuclear ones) were microscopically determined by the neutron diffraction experiment. There are similar rules valid to scatter both - the neutron and the X-ray radiation, i.e. in the case of elastic scattering (which is the only type that we use for purpose of this work to determine the magnetic structures) the neutrons follow the Bragg's law (see chapter 2. Theory). In the equation (2.14) parameter λ is the wavelength of the neutrons used for the experiment. The wavelength is being

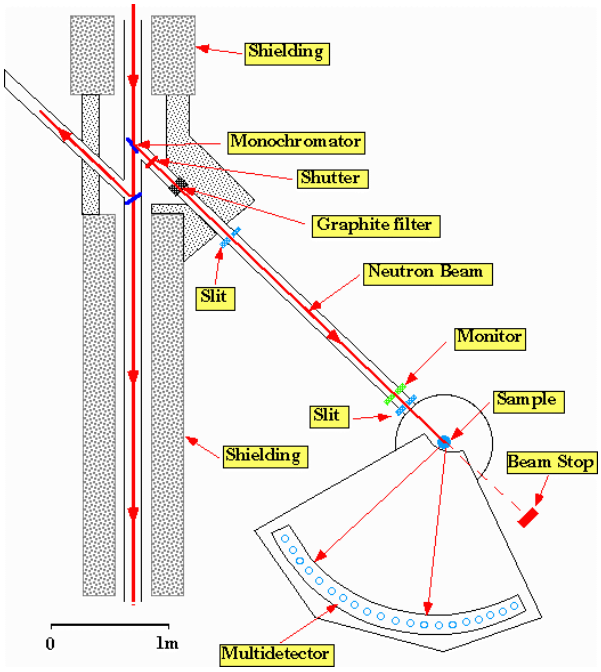

Figure 4.2: The schematic picture of the powder neutron-diffraction experiment arrangement. This figure describes the D1B line in ILL that was mostly used for our polycrystalline-samples studies.

selected from the white beam coming from the source by a monochromator – generally, the crystals like pyrolytic graphite (PG), silicon, beryllium, germanium, copper and other materials set to a reflection condition of a selected reflection can be used as a monochromator. In our case a single crystal in a specific orientation (see Figure 4.2) was used. The monochromatic beam was then scattered by the sample and angular distribution of the scattered neutrons defined the studied material from point of view of the crystalline structure as well as the magnetic structure.

Powder neutron diffraction

A powder neutron diffraction experiment is used to study the polycrystalline samples. In this type of experiment, the neutron beam is scattered by the sample in a powder form. A detector then counts the angular distribution of the diffracted intensities. The banana-type multidetector is used.

The Figure 4.2 shows arrangement of the D1B diffractometer installed in the Institut Laue-Langevin (ILL) in Grenoble that was used for most of our neutron-diffraction experiments performed on powder samples. The initial wavelength of the neutron beam selected by the pyrolytic graphite (002 reflection) was $\lambda_{D1B} = 2.52$ Å. The banana multidetector worked with resolution of 0.2° (400 channels covering the range of 80 degrees). We used a Vanadium holder with the inner diameter of $\phi = 5$ mm to fix the powdered samples of amount approx. 5 g. In case of Dy-based series ($DyNi_{1-x}Cu_xAl$) we had to choose different type of holder due to high absorption caused by the Dy atoms. The special holder (also made of Vanadium) was a double-wall container with the sample space restricted by diameters $\Phi = 9$ mm and $\phi = 8$ mm and the length of 60 mm (see Figure 4.3). We used amounts of approx. 2-3 g in this case. Standard orange cryostat was used for cooling the sample down to the lowest temperature of 1.6 K. The crystal structure and magnetic structure can be then refined by fitting of the model scattering profile to a measured one by various programs (e.g. FullProf [14]) - similar to the X-ray powder diffraction. The neutron scattering form factors for all the

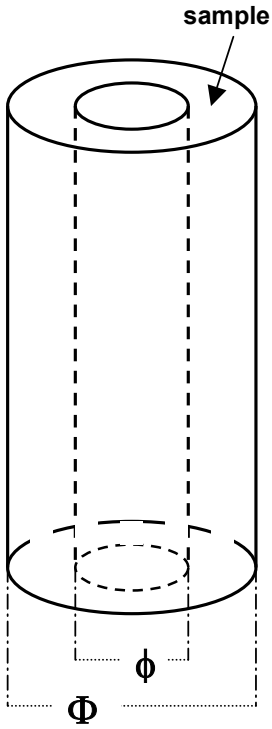

Figure 4.3: The double-wall container used for the neutron diffraction on the Dy-based samples. The powder sample is placed in the tiny space restricted by the two cyllindrical walls with diameters ϕ and Φ.

elements are included in the refinement program. We applied the special correction on the absorption on the data of the Dy-based samples due to the double-wall container that was used specially to reduce the effect of very high absorption of Dy. The correction was applied using the program built up in accordance with the experimental setup [60]. The correction on the Lorentz factor (eq. (2.21)) was performed also in the case of Er-based samples, in this case we could use standard correction (according to eqs. (2.22), see part 2. Theory) that is included in the refinement calculations of the program FullProf [14].

Single-crystal diffraction

The neutron diffraction on a single-crystalline samples can be measured using a four-circle diffractometer or its simplification two-axis diffractometer (see Figure 4.4). The sample is oriented to a specific orientation with respect to the initial beam and the detector can be then moved to exact position corresponding to the studied reflection. On this position the detector either performs some kind of scan (2 theta scan, theta-2theta or ω-scan etc.) to cross the reflection in the reciprocal space (in case of single detector) or the intensity of the diffracted beam is simply counted by a 2D detector (if such a detector is used) to know the intensity of the studied reflection. From the set of measured intensities one can again determine the crystal and magnetic structure. Single-crystal experiment provides usually more information in comparison to powder diffraction where several reflections of the same type fall into the same diffraction angle but in case of single-crystal diffraction these will be observed in different positions symmetrically situated with respect to axis of the initial beam. Thus it can happen that from powder diffraction experiment two or more possible solutions of the magnetic structure will arise but studying of the equivalent reflections – e.g. 100 and 010 in the hexagonal symmetry – one can decide between the two possible arrangements.

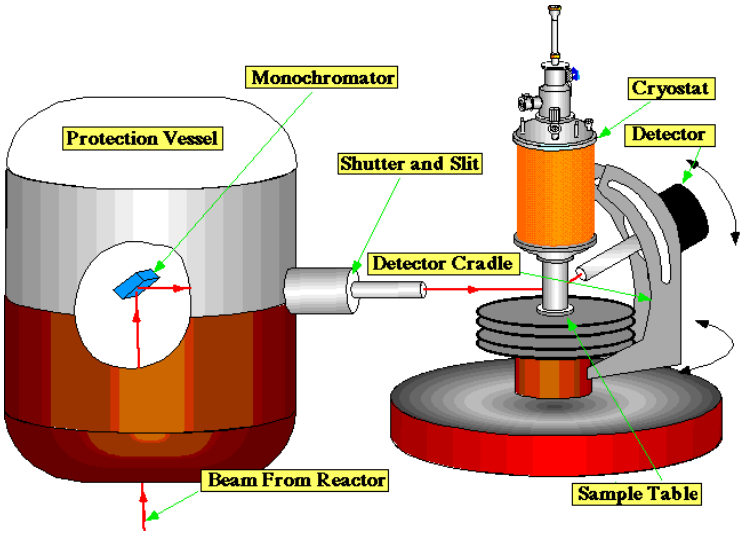

Figure 4.4: The schematic picture of the D15 two-axis diffractometer in ILL Grenoble that was used for our single-crystal diffraction experiment in zero external magnetic field.

For our single-crystal studies on DyNiAl sample we used the two-axis diffractometer D15 in ILL (establishment of the magnetic structure at low temperature and zero external magnetic fields; Figure 4.4) with the initial wavelength of the neutron beam $\lambda_{D15} = 1.17$Å (Cu single-crystal monochromator). The sample of size 1.20 x 1.24 x 1.54 mm^3 was used for the experiment. Program MXD [61] was used for the refinement. The scattering factors and absorption cross-sections tabulated in Reference [12] and the magnetic form factor of Dy^{3+} ions given in Reference [13] were used in the analysis. The crystal structure was refined from intensities of 72 non-equivalent reflections (204 in total) measured at 40 K. No extinction correction was necessary to apply. The correction on the Lorentz factor was done according to the equation (2.21a). Correction on the absorption factor (equation (2.22)) did not bring any difference in the fit. The ferromagnetic component has been obtained by analyzing the same set of reflections at 2K, the AF one by analyzing intensities of 30 non-equivalent (110 in total) reflections at 2K.

For the single-crystal diffraction study under high magnetic field we used the two-axis difractometer E4 operating in Hahn-Meitner Institute Berlin (HMI) with the wavelength of the incident beam $\lambda_{E4} = 2.44$ Å (PG). The measurements performed on the E4 diffractometer (HMI) were performed with the external high-magnetic-field option provided by a superconducting coil with vertical orientation up to 14.5 T. The same piece of the crystal as for zero-field experiment in ILL was used for this measurement. The geometry of the split magnet allowed us to measure only reflections in the horizontal (equatorial) plane. Thus we were restricted to measure only reflections of the (h h l)-type in the "field along *a*-axis" ($H \parallel a$) arrangement and the reflections of the (h 0 l)-type in the "field perpendicular to *a*-axis" ($H \parallel b$) arrangement. All reflections were measured both with increasing and decreasing field, with no intensity difference. Program FullProf [14] was used for the refinement. Due to the geometry of the experimental setup we used the correction on the Lorentz factor in the form of equation (2.21b).

5. Results

The studied compounds were studied from point of view of crystal structure and magnetism. Both ways have brought interesting results. We will deal with the structure and magnetic data separately.

5.1 Crystal structure

The previous structural study of the $ErNi_{1-x}Cu_xAl$ series [55] brought a surprising discovery of a step in the concentration dependence of the lattice constants *a* and *c* between $0.5 \leq x \leq 0.6$. This step was observed at room temperature and also at the low temperature $T = 1.6$ K (neutron diffraction).

Similar step was observed also in the $DyNi_{1-x}Cu_xAl$ series, shifted in the concentration dependence between $0.3 \leq x \leq 0.4$ (this work). Observing previous results done on the $TbNi_{1-x}Cu_xAl$ series [62], which exhibits the same type of step in the structure at room temperature, brings a sign of tendency of the step in the $RNi_{1-x}Cu_xAl$ compounds with respect to the involved *R* element. Moreover, the step in the lattice parameters in the studied compounds has a common parameter – in all the cases the ratio of *c/a* skips the same values from approx. 0.565 to 0.575.

Another study of several compounds crystallizing in the ZrNiAl-type crystal structure showed a step within the evolution of the temperature dependence of the lattice constants. This step can be observed especially for compounds having the ratio of the lattice constants *c/a* close to the critical range as mentioned above (e.g. GdNiAl [63,64], GdPdAl [65,66], TbNiAl [62], TbPdAl [22]). Similar step is also seen when inspecting the *R*NiAl or *R*PdAl series between *R* = Sm and Gd [41]. This brings an idea of a common rule for the *RT*Al compounds crystallizing in this structure type that there is a kind of a "forbidden ratio" of the lattice constants *c/a* that cannot be reached by these compounds. In this section we will describe this effect on the compounds that we have studied and at which we could observe this property.

For the purpose of labelling we will call in further text values of *c/a* below the forbidden region (close to the lower boundary of $c/a \approx 0.565$) as a "low *c/a*" and the values of *c/a* above the step-like change (above the higher boundary of $c/a \approx 0.575$) as a "high *c/a*".

We have also discovered two examples where this rule of forbidden *c/a* ratio region is not complied. In case of the $TbPd_{1-x}Ni_xAl$ series, *c/a* ratio for the compounds with $x = 0.2$, 0.5 and 0.8 at a given temperature fall into the forbidden shell. Also in case of compounds $Ce_{1-x}Y_xPdAl$ with $x = 0.4$ and 0.6 where two coexisting phases were observed at room temperature, one of the two phases also reaches the forbidden value of the *c/a* ratio. We will discuss it in the Chapter 6. Discussion.

5.1.1 ZrNiAl-type structure

The studied materials belong to the group of ternary intermetallic *RTX* compounds crystallizing in ZrNiAl-type hexagonal structure (space group $P\bar{6}2m$; group No. 189; see Figure 5.1a). *R* stays here for a rare-earth metal, *T* is a transition metal and *X* stands for IIIB, IVB or VB group of the Periodic Table of Elements.

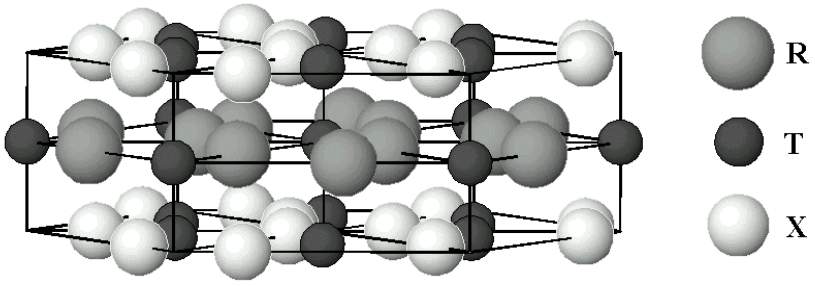

Figure 5.1a: ZrNiAl-type hexagonal structure.

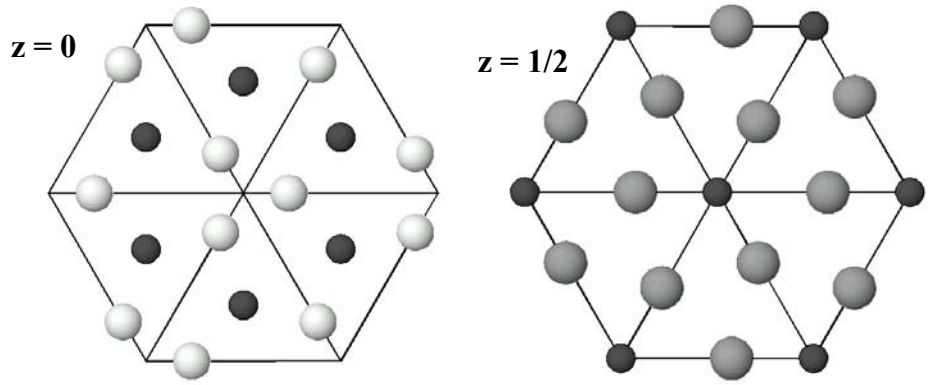

Figure 5.1b: Two types of basal planes in ZrNiAl-type structure.

There are two types of planes in the ZrNiAl-type hexagonal structure (see Figure 5.1b). One type of the basal planes contains the rare earth (*R*) and one out of three atoms of the transition metal (*T*) per unit cell. Two such layers are separated by a non-magnetic layer containing *p*-metal (*X*) and two out of the three transition metal atoms (*T*). These two planes change periodically in the ABAB… sequence. The coordinates of the elements are following:

$3R$: $(X_R,0,½)$, $(0,X_R,½)$, $(-X_R,-X_R,½)$ $\quad$ $1T$: $(0,0,½)$
$3X$: $(X_{Al},0,0)$, $(0,X_{Al},0)$, $(-X_{Al},-X_{Al},0)$ $\quad$ $2T$: $(⅓,⅔,0)$, $(⅔,⅓,0)$

While the positions of transition-metal atoms are fixed, the positions of rare-earth and *p*-metal atoms depend on structure parameters X_R and X_{Al}. Values of these parameters are obtained from X-ray analysis (see Tables 5.1 and 5.2).

As it is seen from the Figure 5.1, each of the R atoms has four nearest neighbours of the similar element in the same basal plane at a distance

$$d = a\sqrt{1 - 3X_R + 3X_R^2} \qquad (5.1)$$

Another two neighbours lie in the nearest plane of the same type at a distance of the lattice constant c. The ratio c/a determines which of these two types of neighbours is the nearest neighbour, eventually.

5.1.2 Effect of substitution

$ErNi_{1-x}Cu_xAl$

The $ErNi_{1-x}Cu_xAl$ pseudoternary series was studied earlier by the X-ray powder diffraction at room temperature and several samples ($x = 0.0$, 0.4, 0.5, 1.0) at low temperatures down to $T = 5$ K (see Chapter 3. Previous results). Based on these data, the structural step, observed at the room temperature between $x = 0.5$ and 0.6, was expected to be kept down to the temperature of at least 5 K. Afterwards, we have performed a neutron-diffraction experiment on these compounds ($x = 0.05$, 0.1, 0.2, 0.4, 0.5, 0.6, 0.8) in temperatures down to $T = 1.6$ K. In addition, another two samples were prepared to complete the picture: $x = 0.3$ and 0.55. The Figure 5.2 displays the X-ray data measured at room temperature in comparison with that ones measured by the neutron diffraction

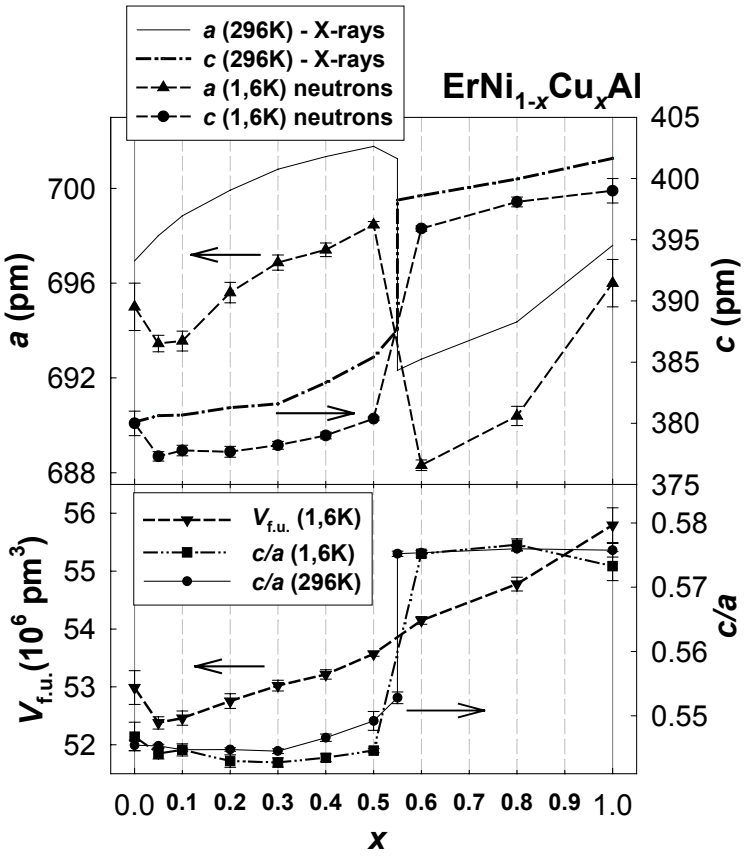

Figure 5.2: The structural discontinuity in the lattice parameters *a,c* in the $ErNi_{1-x}Cu_xAl$ series as studied by X-rays [55] and using the neutron diffraction. The evolution of the lattice-constants ratio *c/a* and of the formula-unit volume $V_{f.u.}$ at room temperature is displayed too. Sample with $x = 0.55$ contains two isostructural phases with different *a* and *c*.

at the lowest studied temperature. Table 1 summarizes the measured parameters at room temperature and at $T = 15$ K by the neutron diffraction (in the paramagnetic state). The change of the lattice between the lowest temperature and 15 K is negligible. One can see that all the data measured by the neutron diffraction keep the character of the step-like evolution of the lattice parameters as it was observed at room temperature.

Although the lattice parameters in this series change step-like, the evolution of the volume keeps the linear evolution following the Veggard's law (see Figure 5.2).

Table 5.1: The lattice parameters of the $ErNi_{1-x}Cu_xAl$ samples at room temperature and at 15 K. The sample with $x = 0.55$ was not measured by neutron diffraction, the low-temperature data were taken from the low-temperature X-ray diffraction measurement at T = 10K.

x	***T = 296 K*** (X-ray data)		***T = 15 K*** (neutron data)				
	***a* (pm)**	***c* (pm)**	X_{Er}	X_{Al}	***a* (pm)**	***c* (pm)**	R_{Bragg}
0[54]	696.9(0.5)	380.1(0.3)	0.584 (3)	0.203(18)	695.0(1.0)	380.0(1.0)	4.9
0.05	698.0(0.1)	380.6(0.1)	0.584 (1)	0.214(05)	693.5(0.4)	377.3(0.4)	3.6
0.10	698.8(0.2)	380.7(0.1)	0.585 (1)	0.213(07)	693.6(0.4)	377.8(0.4)	4.9
0.20	699.9(0.2)	381.3(0.1)	0.585 (1)	0.209(09)	695.6(0.4)	377.7(0.4)	2.1
0.30	700.8(0.2)	381.6(0.2)	0.585 (1)	0.209(09)	696.9(0.3)	378.2(0.3)	5.3
0.40	701.3(0.3)	383.3(0.2)	0.584 (2)	0.209(11)	697.4(0.3)	379.0(0.3)	4.1
0.50	701.8(0.9)	385.4(0.5)	0.583 (4)	0.184(20)	698.5(0.2)	380.4(0.2)	3.8
0.55	701.3(0.4)	387.6(0.4)	-	-	*698.7(0.3)*	*385.9(0.2)*	-
	692.3(0.2)	398.2(0.2)	-	-	*689.0(0.1)*	*397.7(0.1)*	-
0.60	692.8(0.2)	398.6(0.1)	0.584 (1)	0.232(09)	688.3(0.2)	395.9(0.2)	8.5
0.80	694.4(0.2)	399.9(0.1)	0.582 (1)	0.185(09)	690.4(0.4)	398.1(0.4)	5.9
1[54]	697.6(0.5)	401.6(0.4)	0.588 (3)	0.190(23)	696.0(1.0)	399.0(1.0)	5.2

$DyNi_{1-x}Cu_xAl$

The X-ray powder diffraction measurements performed on the $DyNi_{1-x}Cu_xAl$ series discovered a sudden step in the lattice constants (a,c), similar to that one in Er-based series. Nevertheless, in comparison to the Er-system (where the step appears between $0.5 < x < 0.6$), this discontinuity is shifted to lower concentration region of $0.3 < x < 0.4$ in the Dy-based one (see Figure 5.3). Similarly to the Er-based series, this abrupt change is not connected with any step in the volume evolution.

The neutron diffraction experiment confirmed that this behavior is similar in the low temperatures, even in the magnetically ordered state (as will be discussed later). This means that the structural step is being kept down to $T = 1.6$ K (see Figure 5.3), the only difference from the 300 K data is reaching lower absolute values of the lattice constants *a,c* due to the lattice thermal expansion. The Table 5.2 displays the values of the lattice parameters at room temperature and at $T = 40$ K (i.e. in paramagnetic state). The change of the lattice constants between 40 K and 1.6 K is practically negligible. The values of the *c/a* ratio are being kept over all the concentration scale very similar for both – the room temperature and the low temperatures with the only exception around $x = 0.4$ where the step-like behavior is being more pronounced (Figure 5.3). The linearity of the volume evolution is nevertheless not affected by the structural step like in the Er-based series. As it can be seen from the Table 5.2 the values of the internal parameters X_{Dy} and X_{Al} do not change within the concentration scale *x*.

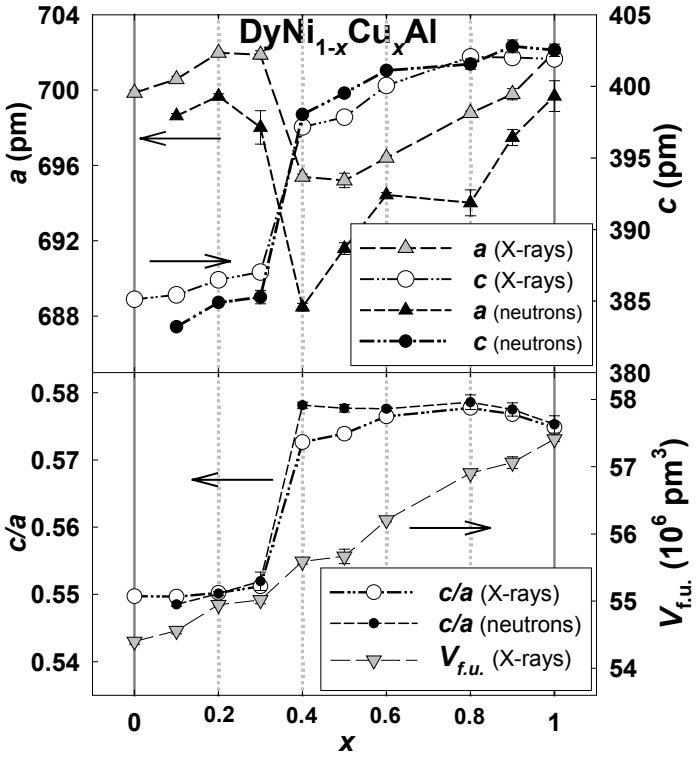

Figure 5.3: The structural parameters *a,c* and calculated ratio *c/a* and volume $V_{f.u.}$ in the $DyNi_{1-x}Cu_xAl$ series as determined from powder X-ray and neutron diffraction.

Table 5.2: The lattice parameters of the $DyNi_{1-x}Cu_xAl$ compounds at room temperature and at 40 K.

x	***T = 300 K*** (X-ray data)		***T = 40 K*** (neutron data)				
	***a* (pm)**	***c* (pm)**	X_{Dy}	X_{Al}	***a* (pm)**	***c* (pm)**	R_{Bragg}
0	699.8(0.2)	384.7(0.1)	-	-	-	-	-
0.1	700.6(0.2)	385.1(0.1)	0.583 (2)	0.225 (14)	697.7(0.4)	384.2(0.3)	7.9
0.2	702.0(0.1)	386.3(0.1)	0.584 (2)	0.229 (13)	698.8(0.4)	385.7(0.2)	4.1
0.3	701.9(0.3)	386.5(0.3)	0.581 (4)	0.237 (30)	698.8(1.1)	386.2(0.6)	13.9
0.4	695.4(0.2)	398.2(0.1)	0.580 (2)	0.219 (17)	689.1(0.6)	398.0(0.3)	4.5
0.5	695.2(0.4)	399.0(0.3)	0.581 (3)	0.200 (24)	692.7(0.8)	399.6(0.4)	7.7
0.6	696.4(0.1)	401.5(0.1)	0.581 (2)	0.199 (14)	694.4(0.5)	401.1(0.3)	4.5
0.8	698.8(0.1)	403.7(0.1)	0.581 (2)	0.201 (17)	694.3(0.6)	401.5(0.3)	4.9
0.9	699.8(0.3)	403.7(0.3)	0.583 (6)	0.238 (62)	697.8(1.5)	402.7(0.8)	6.4
1	702.0(0.1)	403.5(0.1)	0.579 (3)	0.194 (22)	700.5 (0.8)	402.6(0.5)	8.0

$TbNi_{1-x}Cu_xAl$

$TbNi_{1-x}Cu_xAl$ exhibits the structural discontinuity between $x = 0.2$ and 0.3 at the room temperature (see Figure 5.4 and Table 5.3), as already observed by Ehlers in his thesis [62]. Our low-temperature X-ray diffraction study of this series discovered that below 200 K the transition is shifted to range between $x = 0.0$ (TbNiAl) and 0.1, and at $T < 90$K there is no structural step in Cu-concentration dependence – in accordance with statement of Ehlers at $T = 60$ K in [3]. The step within the temperature dependence of compounds with $x = 0.0$, 0.1 and 0.2 will be discussed later.

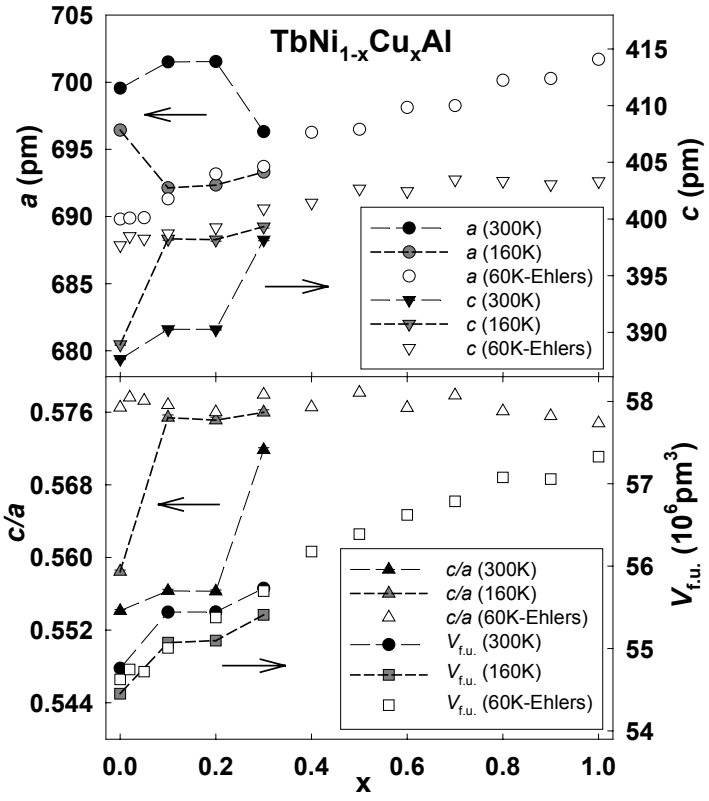

Figure 5.4: The structural parameters *a,c* and calculated *c/a* ratio and volume $V_{f.u.}$ in the $TbNi_{1-x}Cu_xAl$ series as determined from X-ray powder diffraction. The data at 60 K are taken from [3].

Table 5.3: The lattice parameters of the $TbNi_{1-x}Cu_xAl$ compounds for $0.0 \le x \le 0.3$ at room temperature, at T = 160 K and at T = 8 K as measured by X-ray diffraction.

x	***T* = 300 K**		***T* = 160 K**		***T* = 8 K**	
	***a* (pm)**	***c* (pm)**	***a* (pm)**	***c* (pm)**	***a* (pm)**	***c* (pm)**
0	699.5(0.1)	387.6(0.1)	696.4(0.1)	388.9(0.1)	688.3(0.2)	397.3(0.1)
0.1	701.5(0.1)	390.3(0.1)	692.1(0.2)	398.2(0.1)	689.8(0.1)	399.2(0.1)
0.2	701.5(0.1)	390.2(0.1)	692.3(0.2)	398.2(0.1)	690.0(0.3)	398.3(0.2)
0.3	696.3(0.2)	398.2(0.1)	693.3(0.2)	399.3(0.1)	691.3(0.1)	400.1(0.1)

$Ce_{1-x}Y_xPdAl$

Another type of substitution – on the rare-earth position – was studied too. We were dealing with the $Ce_{1-x}Y_xPdAl$ series. The evolution of crystal-lattice parameters *a* and *c* – as well as their ratio *c*/*a* and volume per formula unit $V_{f.u.}$ – is displayed in the Figure 5.5 and in Table 5.4. Increasing the Y content leads to appearance of the splitting of several diffraction peaks in the X-ray diffraction pattern within the region of $0.4 \le x \le 0.6$. Careful study of the diffraction patterns in this Y-concentration range (Figure 5.6) leads to estimation that this effect is caused by

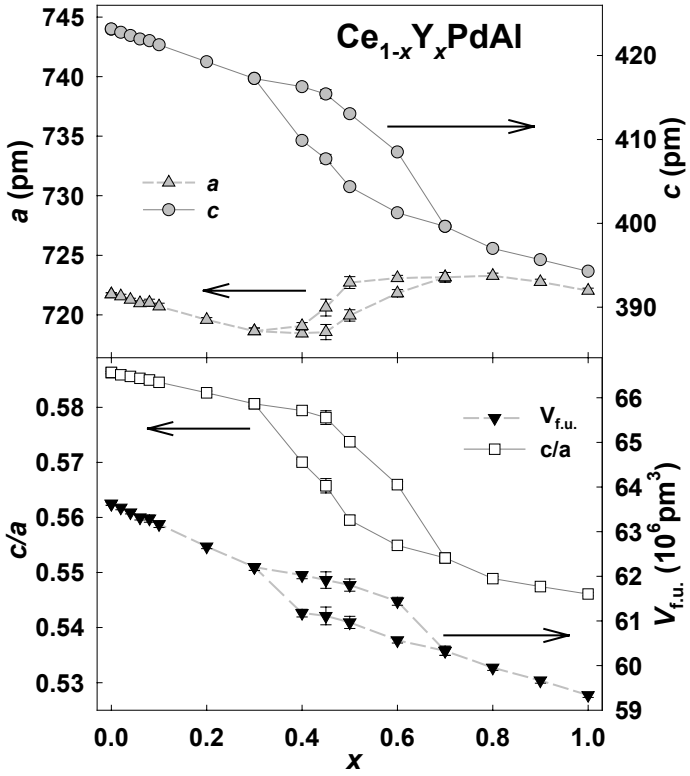

Figure 5.5: The evolution of the lattice constants *a*,*c* their ratio *c*/*a* and the volume of the formula unit $V_{f.u.}$ in the $Ce_{1-x}Y_xPdAl$ compounds as the dependence on the substitution parameter *x* at room temperature.

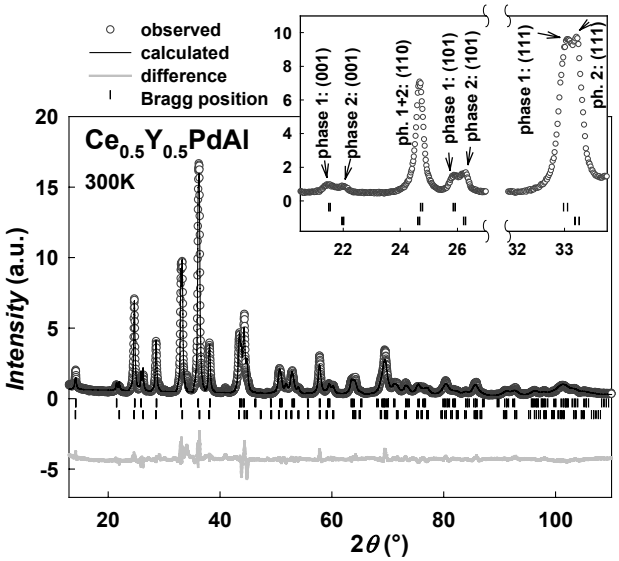

Figure 5.6: The X-ray diffraction pattern of the $Ce_{0.5}Y_{0.5}PdAl$ as an example of the two-phase compound. The splitting of several reflections can be visible on the insight picture.

Table 5.4: The structural parameters of the $Ce_{1-x}Y_xPdAl$ compounds at 300 K.

x	*a* (pm)	*c* (pm)
0.0 (CePdAl)	721.7 (2)	423.1 (1)
0.02	721.6 (2)	422.8 (1)
0.04	721.6 (2)	422.4 (1)
0.06	721.0 (2)	422.0 (1)
0.08	721.0 (3)	421.8 (2)
0.1	720.7 (3)	421.3 (2)
0.2	719.6 (2)	419.3 (1)
0.3	718.6 (3)	417.3 (2)
0.4	718.4 (3)	416.3 (2)
	719.1 (3)	409.9 (2)
0.45	718.6 (6)	415.4 (5)
	720.6 (7)	407.7 (5)
0.5	719.9 (5)	413.1 (4)
	722.7 (5)	404.4 (3)
0.6	721.8 (3)	408.5 (2)
	723.1 (2)	401.3 (1)
0.7	723.2 (4)	399.6 (2)
0.8	723.3 (2)	397.0 (1)
0.9	722.8 (2)	395.7 (1)
1.0 (YPdAl)	722.0 (2)	394.3 (1)

appearance of another hexagonal ZrNiAl-type phase in these compounds. Samples with $x > 0.6$ already show only single-phase pattern again. The evolution of the volume in the critical region of the x-dependency exhibits splitting.

5.1.3 Temperature evolution

TbNiAl

For TbNiAl compound we have observed the structural step in the temperature evolution of the lattice parameters a and c (see Figure 5.7).

The c/a values, obtained from the temperature dependence of lattice constants in the TbNiAl, skip comparable c/a values, as in the case of RNi$_{1-x}$Cu$_x$Al (R = Dy, Er, Tb) compounds - i.e. ≈ 0.565-0.575 (see Figures 5.2, 5.3, 5.4).

In the transient temperature region between $95 \leq T \leq 120$ K, two isostructural phases with distinctly different c/a values coexist (similar to that one in the Ce$_{1-x}$Y$_x$PdAl series): one giving c/a above (high c/a) and another one resulting in c/a below (low c/a) the "forbidden region", respectively. The typical evolution of selected reflections in the powder pattern with respect to temperature is shown in Figure

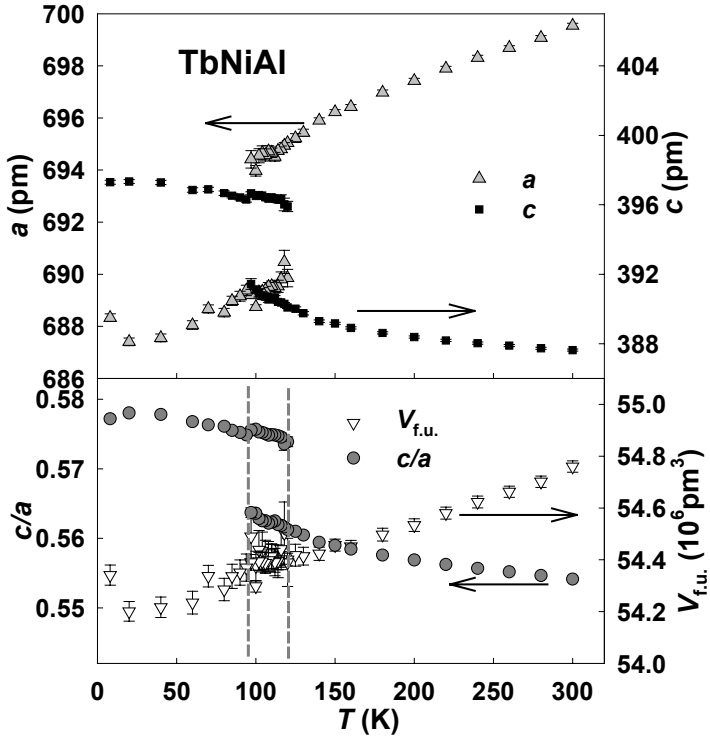

Figure 5.7: The temperature dependence of lattice parameters in the TbNiAl compound. The coexistence region observed in small temperature range is marked by two vertical dashed lines.

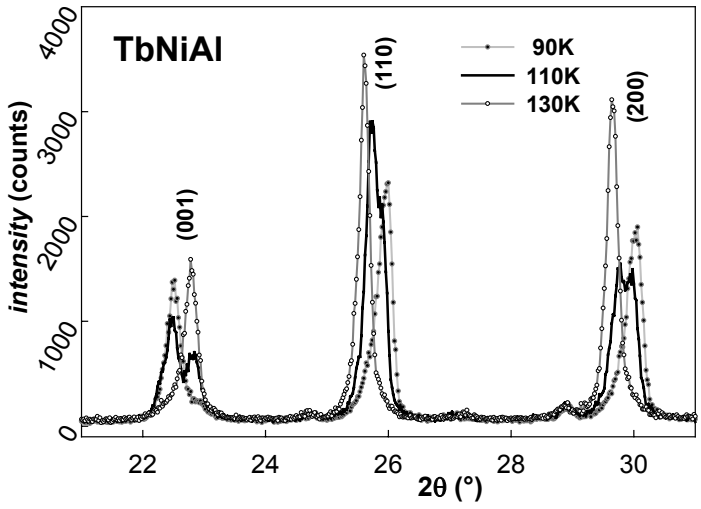

Figure 5.8: Parts of the diffraction patterns of TbNiAl at temperatures below-, above- and inside the coexistence region, respectively. A clear splitting of (001) and (200) reflections can be seen in the 110 K pattern.

5.8 - in the transient temperature interval one coexisting phase ($c_1/a_1 \approx 0.575$) expands on account of the other ($c_2/a_2 \approx 0.563$).

$TbNi_{1-x}Cu_xAl$

$TbNi_{0.9}Cu_{0.1}Al$ and $TbNi_{0.8}Cu_{0.2}Al$ compounds exhibit similar structural step like that one observed in TbNiAl. In these compounds the step can be observed between $T = 200$ K and 250 K (see Figure 5.9), i.e. in higher temperatures than the TbNiAl compound. The transition from the high *c/a* phase to the low *c/a* phase happens through consequent raising of new phase on the account of the previous one, so in the transient temperature region the coexistence of both phases is present. The $TbNi_{0.7}Cu_{0.3}Al$ sample exhibits the values of the *c/a* ratio already all in the region of "high *c/a* ratio".

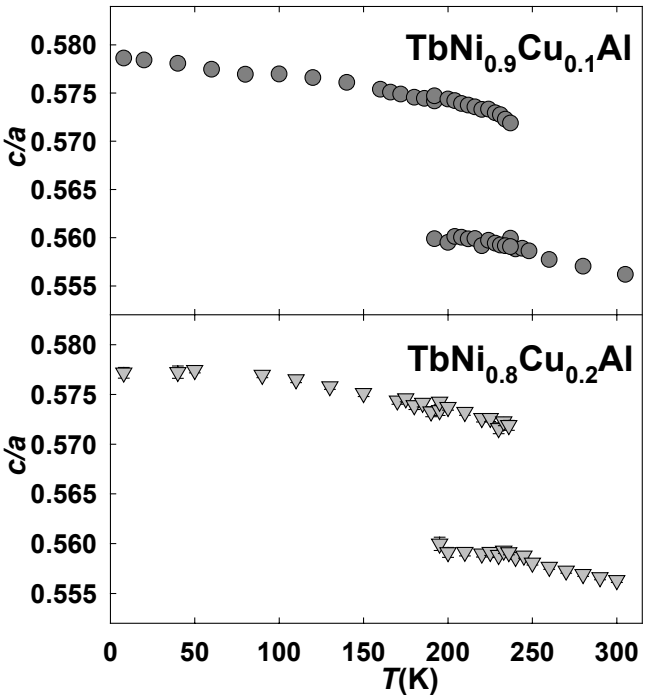

Figure 5.9: Temperature dependence of the lattice-constants ratio *c/a* in two $TbNi_{1-x}Cu_xAl$ samples (x = 0.1 and 0.2).

$ErNi_{0.45}Cu_{0.55}Al$

Special case in the $ErNi_{1-x}Cu_xAl$ series is the compound with $x = 0.55$ that was prepared in order to approach to the point of the structural step. This sample exhibits coexistence of two isostructural phases at room temperature, which survives down to

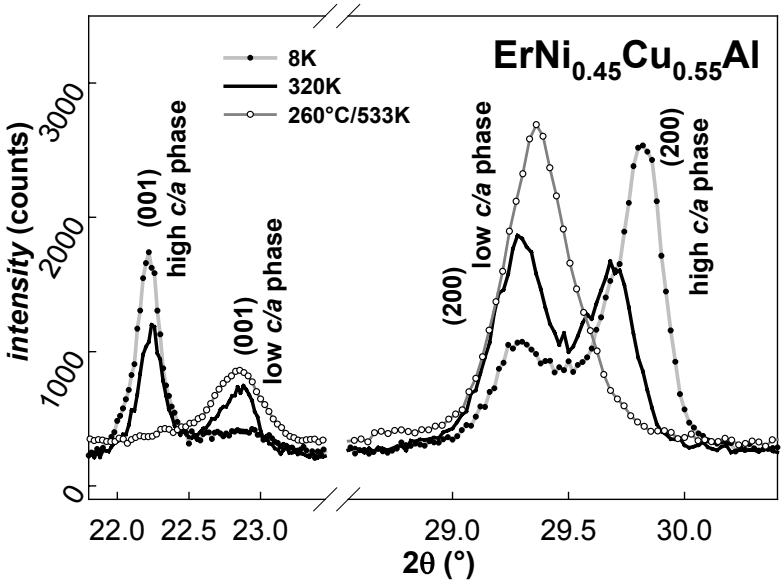

Figure 5.10: The diffraction patterns of the $ErNi_{0.45}Cu_{0.55}Al$ compound exhibiting the two-phase coexistence. The patterns are focused on reflections that split in the coexistence region most significantly.

low temperatures (7.5 K). First assumptions that this sample cannot be prepared as a single-phase compound – due to being on boundary of the structural transformation (see sec. 5.1.2) – were suppressed by additional measurements of high-temperature X-ray diffraction. Although the sample consists of two isostructural phases over wide temperature range from room temperature down to 7.5 K at least, it becomes single-phase at higher temperatures, namely above 220°C (~ 493 K) the diffraction pattern contains already only one set of peaks (see Figure 5.10). It is worthy to mention that this effect is reversible, i.e. after cooling down below 220°C it becomes two-phase again.

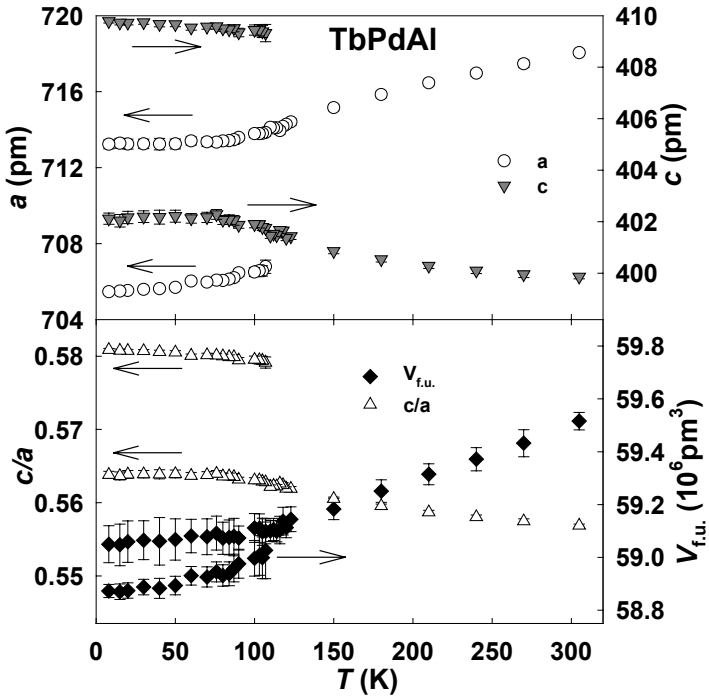

Figure 5.11: Temperature dependence of the lattice parameters of the TbPdAl compound.

$TbPd_{1-x}Ni_xAl$

Several samples from the $TbPd_{1-x}Ni_xAl$ series were also studied from the structural point of view. A similar coexistence of both phases – the high *c/a* and low *c/a* phase – like that one observed in the TbNiAl compound (see above) was observed for TbPdAl. In this case the coexistence was found over much broader ($8 \leq T \leq 110$ K) temperature interval; (see Figure 5.11) even broader than reported by Dönni [22].

The small Ni substitution ($x = 0.1$) for Pd yields further extension of the transient temperature region of the two-phase coexistence covering the entire temperature range of our experiments, namely 8–310 K

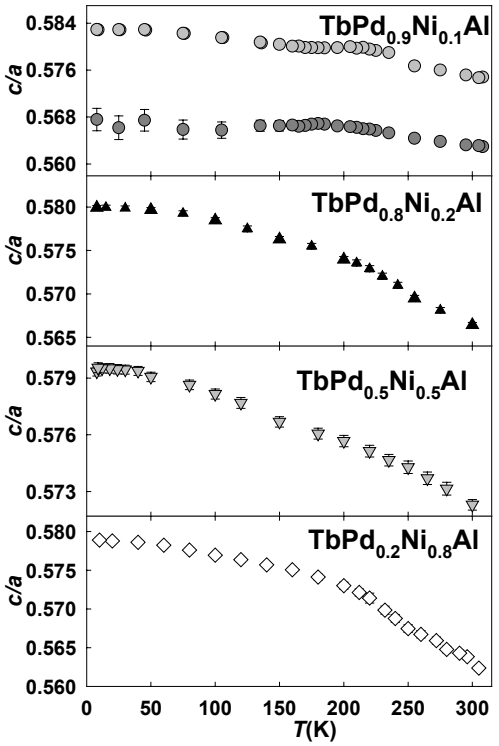

Figure 5.12: Temperature dependence of the *c/a* ratio of the $TbPd_{1-x}Ni_xAl$ compounds (x = 0.1, 0.2, 0.5, 0.8).

(Figure 5.12). On the contrary, samples with the Ni substitution of $x = 0.2$, 0.5, 0.8 surprisingly show continuous temperature dependence of lattice parameters and consequently the *c/a* ratio passes through the "forbidden region" (see also Figure 5.12).

5.2 Magnetism

The previous investigations of magnetic properties of the pseudoternary series $ErNi_{1-x}Cu_xAl$ based on bulk measurements are given in Ref. [4]. ErNiAl and ErCuAl compounds order antiferromagnetically below $T_N = 6.2$ K and ferromagnetically below $T_C = 6.8$ K, respectively. Besides the change of type of magnetic order also reorientation of the magnetic moments and change of magnetocrystalline anisotropy was expected. The magnetization and heat capacity measurements brought a picture of consequent change from antiferro- to ferromagnetic order between $0.05 \leq x \leq 0.2$ and the compounds with $x \geq 0.4$ ordering ferromagnetically. Our new results, presented here, are based on the neutron diffraction experiment. We have discovered more complicated magnetic structures with antiferromagnetic order within the basal plane for compounds with $0.05 \leq x \leq 0.4$, additionally the incommensurate antiferromagnetic propagation for the compounds with $0.2 \leq x \leq 0.4$, ferromagnetic order for the $ErNi_{0.5}Cu_{0.5}Al$ compound and signs of short-range magnetic order for compounds with $x = 0.6$ and 0.8.

The $DyNi_{1-x}Cu_xAl$ samples were studied consequently after getting the results on the Er-based series. After succeeding to grow a DyNiAl single crystal we have studied the magnetic properties of the single crystalline sample of DyNiAl as the parent compound of the $DyNi_{1-x}Cu_xAl$ series. Only simple ferromagnetic phase was observed below $T_C = 30$ K down to $T_1 = 15$ K. In the low-temperature phase below T_1, the magnetic structure consists of ferromagnetic component oriented along the hexagonal *c*-axis and antiferromagnetic component lying within the basal plane. There were several field-induced transitions observed on the magnetization curves. The magnetic structure under high magnetic fields up to 14.5 T was also studied using neutron diffraction when the field was applied along *a* and along *b* (perpendicular to *a*) axis, respectively.

In the substitutional Dy-based series the question of magnetic evolution within the pseudo-ternaries with similar behavior of the parent compounds should be answered. Even in this case, the short-range order is still present and the evolution of magnetic order was found to be surprisingly complicated, what could be observed with both – bulk and microscopic methods. The compounds with $x = 0.1$ and 0.2 keep the combination of the antiferromagnetic and ferromagnetic order at the lowest temperature of 1.6 K with similarity to the parent DyNiAl. The magnetic structures of compounds with $x \geq 0.4$ consist of just one magnetic component: incommensurate antiferromagnetic for $x = 0.4$, simple antiferromagnetic for $x = 0.5$ and 0.6 and simple ferromagnetic for $x = 0.9$ and 1.0. For $x = 0.8$ no long-range magnetic order was observed.

The phase-transition temperatures were determined preferably form the bulk measurements. The accuracy is less precise for the neutron diffraction experiment, especially in the $DyNi_{1-x}Cu_xAl$ case, because it is not always clear when the intensity of

the reflection starts to increase. Relatively larger temperature step in the neutron experiments is other reason.

5.2.1 $ErNi_{1-x}Cu_xAl$

$x = 0.05$ and 0.1

The results of bulk measurements performed on the $ErNi_{1-x}Cu_xAl$ samples with $0.05 \leq x \leq 0.2$ found two anomalies in the temperature dependencies [4]. Using the neutron diffraction experiment performed on these compounds we have found out that the lower ones are connected probably with just subtle change of magnetic structure leaving the propagation vector unchanged. The Figure 5.13 displays the temperature dependence of neutron-diffraction intensities of selected reflections in the $ErNi_{0.95}Cu_{0.05}Al$ in comparison with the bulk data as measured earlier [4]. The magnetic structure of compounds with $x \leq 0.10$ can be described by the only propagation vector (p.v.) $\boldsymbol{k}_1 = (½\ 0\ ½)$, similar to that in parent ErNiAl compound [54]. We first tried to fit the data obtained for $x = 0.05$ compound with a magnetic structure of ErNiAl (erbium moments aligned along the crystallographic directions, containing 60 or 120 degrees with each other and creating thus a triangle-like structure – see 3. Previous results), that is in agreement with results of group theory [67]. The fit to the $ErNi_{0.95}Cu_{0.05}Al$ data was not satisfactory, we obtained an agreement factor of $R_{mag} = 33\%$. The agreement can be improved when leaving the angles between the moments and crystallographic directions as free parameters during the fitting procedure, i.e. allowing the moments to rotate within the basal plane (see Figure 5.14a). By this

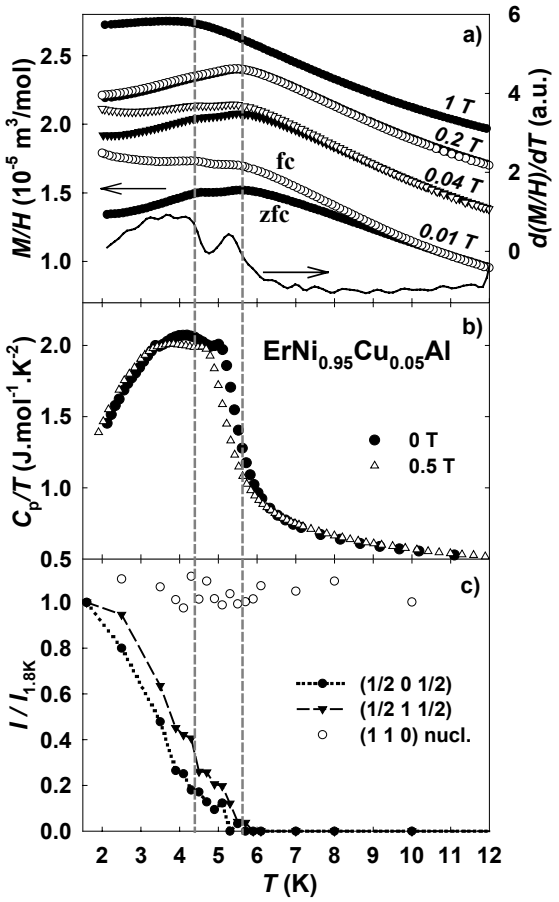

Figure 5.13: Temperature dependence of magnetization (a), heat capacity (b) and selected reflections from the neutron-diffraction experiment (c) for the $ErNi_{0.95}Cu_{0.05}Al$ sample. The vertical dashed lines represent the phase transitions as drived from the heat-capacity data. The data displayed in the (a) and (b) parts are taken from previous study [4].

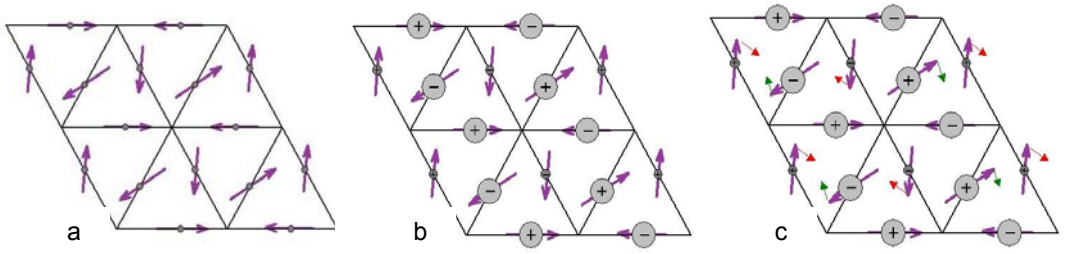

Figure 5.14: The arrangement of magnetic moments in the $ErNi_{1-x}Cu_xAl$ compounds for x = 0.05 and 0.1 (a) within the basal (*a,b*) plane. For 0.2 ≤ x ≤ 0.4 additional antiferromagnetic component parallel to the crystallographic *c*-axis starts to appear with frustrated moment on the (0, X_{Er}, ½) position (b). With increasing x-content (from 0.1 up to 0.4) the magnetic moments intend to rotate clockwise as it is displayed on the last picture (c).

way of refinement we obtained an agreement factor of R_{mag} = 4.8%, when the magnetic moments contain following angles with the crystallographic *a*-axis: 1(7)°, 88(7)° and 34(6)° at (X_{Er}, 0, ½), (0, X_{Er}, ½) and (-X_{Er}, -X_{Er}, ½), respectively. Fit with any other magnetic structure that would be consistent within the group theory does not give a good agreement with observed data (R_{mag} ≥ 33%).

Similar results are obtained for compounds with x = 0.10 and 0.20 but the deviation from the "ErNiAl-type" arrangement becomes gradually more significant. The fit with the ErNiAl magnetic structure gives R_{mag} = 42% and 70%, respectively. The angles of the moments after releasing their basal-plane rotation (on the position (0, X_{Er},½)/(-X_{Er},-X_{Er},½)) decrease down to 80(15)°/20(12)° (R_{mag} = 7.6%) for x = 0.10. The direction of the moment on the position (X_{Er}, 0, ½) is in all the cases stable around the value of 0°. This arrangement of the basal-plane components persists up to x = 0.40, but the quantitative analysis is less reliable due to low magnitudes of the moments (low diffraction intensities).

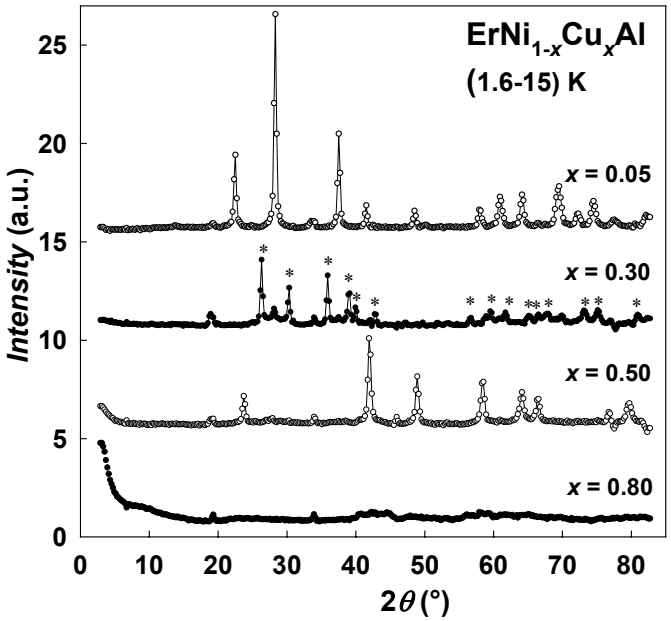

Figure 5.15: The neutron-diffraction difference patterns between 1.6 and 15 K obtained for selected compounds. The reflections marked with "*" (in x = 0.30) belong to the incommensurate propagation. The data are shifted by difference of 5 a.u. for better view. The line is to guide the eye.

x = 0.2, 0.3 and 0.4

The angles of the moments for sample with $x = 0.2$ with released the basal-plane rotation (on the position $(0, X_{Er}, ½)/(-X_{Er},-X_{Er},½)$) is 47(40)°/22(30)°. For compounds with $x \geq 0.3$ the basal-plane component is getting weaker and the accuracy of the angles determination is getting worse. The fit can be improved by allowing the moments at $(0, X_{Er}, ½)$ to have different magnitude (R_{mag} = 9.6%; see Table 5.5).

For samples with *x* from the range 0.20 ÷ 0.40, we observe besides the (½ 0 ½) reflections additional magnetic intensities (see Figure 5.15), that can be indexed by an incommensurate (IC) propagation vector $\boldsymbol{k}_2$ = (½ 0 q), where q = 0.469, 0.425 and 0.427 of reciprocal lattice unit for *x* = 0.2, 0.3 and 0.4, respectively. The intensities of these peaks gradually increase whereas the "$\boldsymbol{k}_1$" reflections become simultaneously weaker (see Figure 5.16). Our analysis of the pattern for *x* = 0.40 yields the picture of longitudinal amplitude-modulated structure with the Er-moments aligned along the *c*-axis (R_{mag} = 11%). One third of the moments (at $(0, X_{Er}, ½)$ for $\boldsymbol{k}_2$ given above) are strongly reduced becoming nearly negligible. This resembles the high temperature magnetic phase of TbNiAl [67], although the propagation in TbNiAl is commensurate. This IC component is present also in compounds with *x* = 0.20 and 0.30 with a somewhat worse agreement (R_{mag} = 18% and 12%, respectively) due to lower intensities.

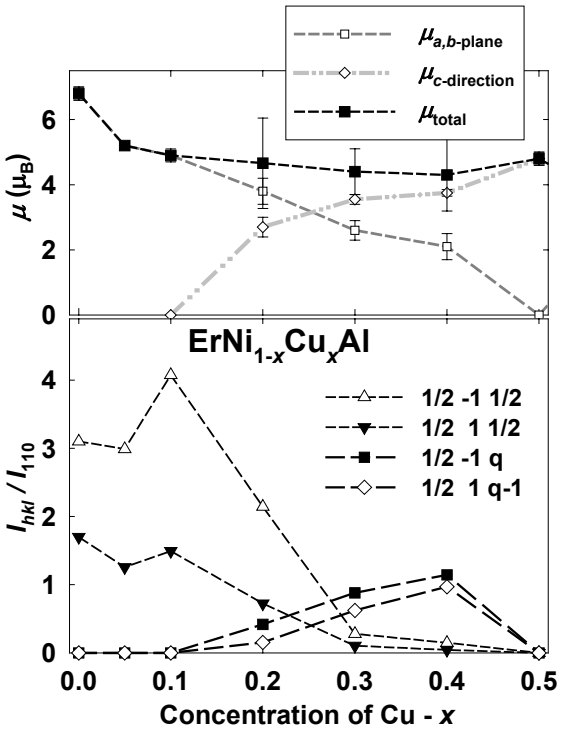

Figure 5.16: Concentration dependence of selected reflections (lower part) belonging to the commensurate ($\boldsymbol{k}_1$ = (½ 0 ½)) and incommensurate ($\boldsymbol{k}_2$ = (½ 0 q)) magnetic structure in the lower concentration region ($x \leq 0.5$). The appropriate components (parallel or perpendicular to the *c*-axis) of the magnetic moment (upper part) are added. For the incommensurate structure the mean value of the moment-component was taken.

x = 0.5

In the $ErNi_{0.5}Cu_{0.5}Al$ compound, the antiferromagnetic reflections completely disappear and only additional intensities on top of the nuclear reflections can be observed at low temperatures. Analysis of the pattern at 1.6 K leads to a magnetic structure with a collinear

ferromagnetic alignment of Er-moments parallel to the *c*-axis ($\mu_{Er} = (4.8 \pm 0.2)\ \mu_B$, $R_{mag} = 6.8\%$).

x = 0.6 and 0.8

A qualitatively different behavior is observed for $x = 0.6$ and 0.8. Only very weak magnetic reflections corresponding to $\boldsymbol{k} = (½\ 0\ ½)$ appear in the $x = 0.6$ sample, which prevents determination of magnetic structure (our best fit of the data leads to the magnitude of the moments $3.2(9)\ \mu_B$ with $R_{mag} = 23\%$). For $x = 0.8$, no magnetic reflections have been detected down to 1.6 K and only an enhanced bumps around possible ferromagnetic reflections have been observed. For both concentrations a large intensity appears at low angles, probably owing to short-range correlations that manifest themselves around the (0 0 0) reflection (see Figure 5.15).

The Table 5.5 contains summary of magnetic data on the $ErNi_{1-x}Cu_xAl$ series. We shall mention that all our final fits were obtained assuming zero magnetic moments on Ni-atoms. Allowing these moments to be nonzero brings no improvement of the fit. Such estimation was result of any other *R*NiAl compound [2,48,68].

Table 5.5: Summary of magnetic properties for the $ErNi_{1-x}Cu_xAl$ series. The parameters μ_{eff} and θ_p and phase-transition temperatures were taken from previous study [4], the parameters of magnetic structures were obtained from neutron diffraction at 1.8 K. The mean values of moments are given in the case of IC structure. Concentrations *x* = 0.60 and 0.80 exhibit signs of short-range ordering (SRO).

x	μ_{eff} (μ_B)	θ_p (K)	T_{ord} (K)	T_1 (K)	μ_{Er} (μ_B)	p.v.	type	R_{mag} (%)
0.0[54]	9.59	-0.3	6.2	4.2	6.8 (2)	(½ 0 ½)	AF ⊥ *c*	6.8
0.05	9.67 (3)	-1.0 (5)	5.7 (2)	4.3 (2)	5.2 (1)	(½ 0 ½)	AF ⊥ *c*	4.8
0.10	9.64 (7)	-2.3 (1.1)	4.9 (2)	4.4 (2)	4.9 (1)	(½ 0 ½)	AF ⊥ *c*	7.6
0.20	9.73 (4)	-1.2 (7)	4.9 (2)	2.8 (3) (weak)	3.8 (5) 2.1 (1.6)* 2.7 (3) 0.2 (6)*	(½ 0 ½) (½ 0 0.469)	AF ⊥ *c* AF ∥ *c*	9.6 18
0.30	9.71 (1)	1.0 (3)	5.0 (2)	—	2.6 (3) 0.3 (1.2)* 3.5 (1) 0.4 (3)*	(½ 0 ½) (½ 0 0.425)	AF ⊥ *c* AF ∥ *c*	14 12
0.40	9.70 (3)	-0.6 (6)	5.1 (2)	—	2.1 (4) 0.0 (1.0)* 3.8 (1) 0.1 (2)*	(½ 0 ½) (½ 0 0.427)	AF ⊥ *c* AF ∥ *c*	12 11
0.50	9.70 (4)	-1.2 (6)	5.8 (2)	—	4.8 (2)	(0 0 0)	F ∥ *c*	7.2
0.60	9.68 (3)	0.2 (4)	4.3 (2)	—	3.2 (9)	(½ 0 ½) & SRO	AF	23 —
0.80	9.56 (3)	0.7 (5)	5.3 (4)	—		SRO		—
1.0[54]	9.55	4.2	6.8	—	6.7 (2)	(0 0 0)	F ∥ *c*	3.2

* magnitude of frustrated moment at position: 0 X_{Er} ½

5.2.2 DyNiAl

The DyNiAl single crystal was studied in framework of the $DyNi_{1-x}Cu_xAl$ series as one of parent compounds. Since it is the only single crystalline sample, we will deal with its detailed study separately.

Paramagnetic region

In the paramagnetic range, the magnetic susceptibility of DyNiAl obeys the Curie-Weiss law (see Figure 5.17; eq. 5.2) with effective magnetic moment $\mu_{eff} = 10.65\ \mu_B$, which corresponds very well to the free Dy^{3+} ion value. The paramagnetic Curie temperatures corresponding to field applied along the *b* and *c* axes are equal to $\theta_p^b = 11$ K and $\theta_p^c = 46$ K, respectively. The difference $\Delta\theta_p = 35$ K is comparable with anisotropy in the ground state (70 K). No anisotropy is observed within the basal plane.

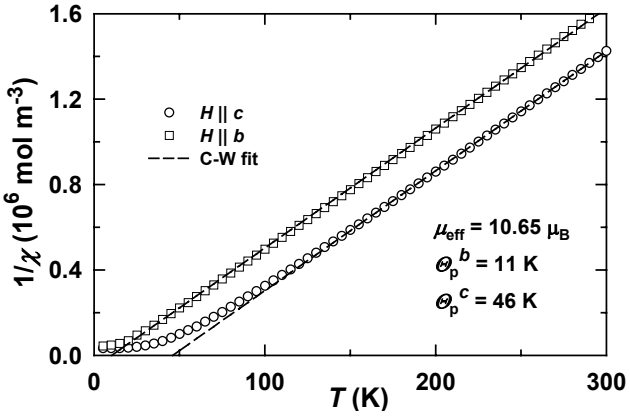

Figure 5.17: Temperature dependence of the magnetic susceptibility in the paramagnetic region.

$$\chi = \frac{M}{H} = \frac{N_A \mu_0 \mu_B^2 \mu_{eff}^2}{3k_B(T-\theta_p)} = \frac{C}{(T-\theta_p)} \ . \qquad (5.2)$$

Bulk measurements at low temperatures

Our magnetization measurements at low temperatures (see Figure 5.18 and 5.20) confirmed generally the results of previous studies on polycrystals and revealed in addition a strong uniaxial magnetic anisotropy and field-induced phase transitions in fields applied perpendicular to *c*-axis. The ordering (Curie) and phase-to-phase ordering temperature is 30 K and 15 K, respectively. The spontaneous

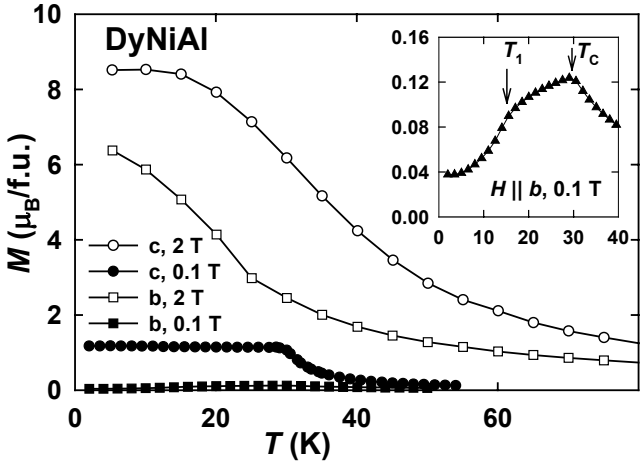

Figure 5.18: Temperature dependence of the magnetic moment *M* for *H* || <120> (*b*) and *H* || <001> (*c*) in a DyNiAl single crystal. The inset shows the low-field curve along the *b*-axis at larger scale. The arrows indicate the magnetic phase transitions.

magnetic moment M_s along the *c*-axis reaches 8.5 μ_B per formula unit at 1.8 K, considerably smaller value than the moment of the free Dy^{3+} ion (10 μ_B). It approaches this value only at ~ 40 T [69] (see Figure 5.19).

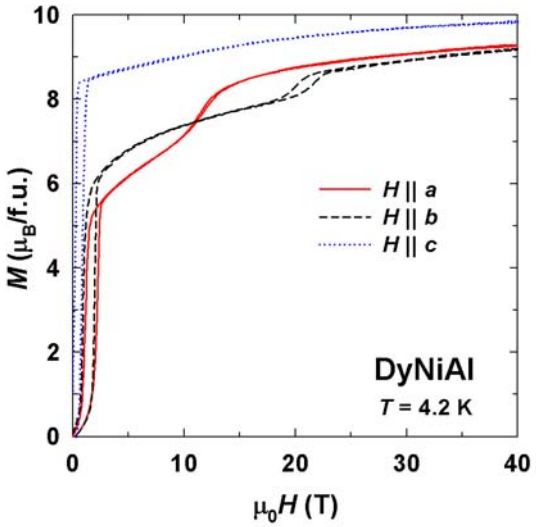

Figure 5.19: Magnetization curves of DyNiAl along all axes at 4.2 K. The figure is taken from literature [69].

Applying magnetic field in the basal plane, we observe the low initial susceptibility what reflects the strong uniaxial anisotropy with anisotropy field estimated as 25 T at 4.2 K (which corresponds to the anisotropy energy ~70 K in the k_BT representation). Field-induced transitions are observed at 1.5 T to 5.5 μ_B for the $H \parallel a$ (<100>direction) and to 6.5 μ_B for the $H \parallel b$ (<120>direction) (see Figure 5.19). The difference indicates a considerable intra-plane anisotropy. The magnetic states resulted at these first-order field-induced phase transitions are stable in a wide interval of further increasing field. Measurements in pulsed-magnetic fields up to 40 T (see Figure 5.19) showed the additional transitions in the basal plane in the fields of 11-13 T and 20-22 T for field applied along the *a*-axis ($H \parallel a$) and along the *b*-axis ($H \parallel b$) at 4.2 K [69]. The transition in the $H \parallel a$ configuration was studied in more detail in steady magnetic fields (see Figure 5.20).

One can see that the magnetization change across the transition around 1.5 T gradually decreases with increasing temperature. The important feature of the transition is that it occurs both below and above T_1. We can exclude its

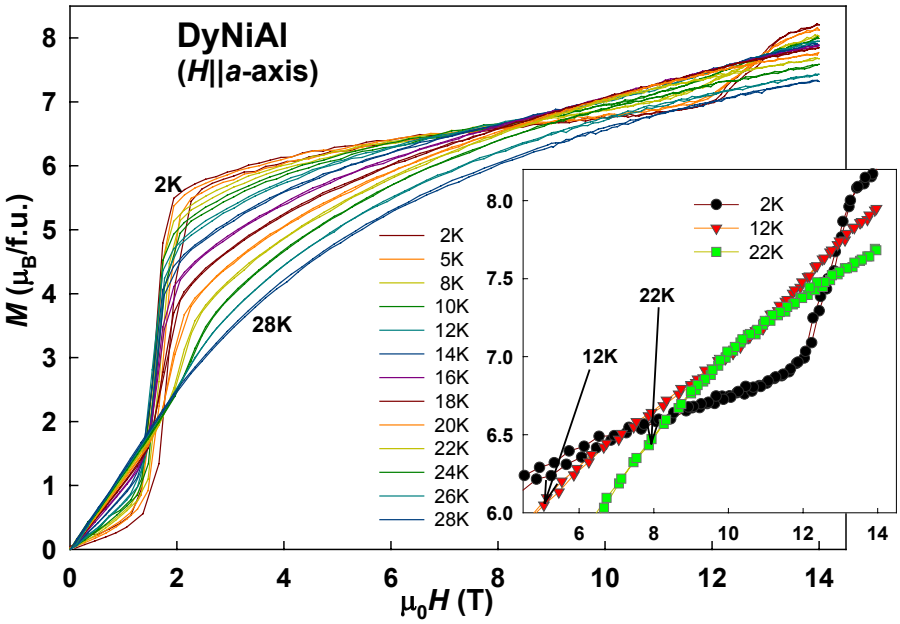

Figure 5.20: The magnetization curves of DyNiAl in the $H \parallel a$ configuration at various temperatures.

metamagnetic nature because above T_1 there is no antiferromagnetic component of the magnetic structure; the compound is a collinear uniaxial ferromagnet. Therefore, we can consider the transition as a rotation of the total magnetic moment from the *c*-axis to a canted structure, which is stable in a wide interval of further increasing field. According to the classification given in [70], the above-mentioned transition is defined as a first-order magnetization process of P2 type. Moreover, the absence of a hysteresis of the transition and the broadening of the transition above T_1 points to its second-order character contrary to the clear first-order one in the low temperature phase.

The additional transition in high fields around 11-13 T applied along the *a*-axis is wider and with smaller magnetization changes across the transition (see the inset of Figure 5.20). The transition is clearly connected with antiferromagnetic component because it disappears above T_1. Despite a small hysteresis observed at 2 K on the magnetization curve in field around 11-13 T, the transition in the higher field is most probably of second order and means a spin-flop of antiferromagnetic component of the magnetic moment. The values of magnetic moment reached above the high-field transitions are still noticeably lower than along the *c*-axis in the same field (~8.5 μ_B for $H \parallel a,b$ and 9.5 μ_B for H $\parallel$ *c* [69]).

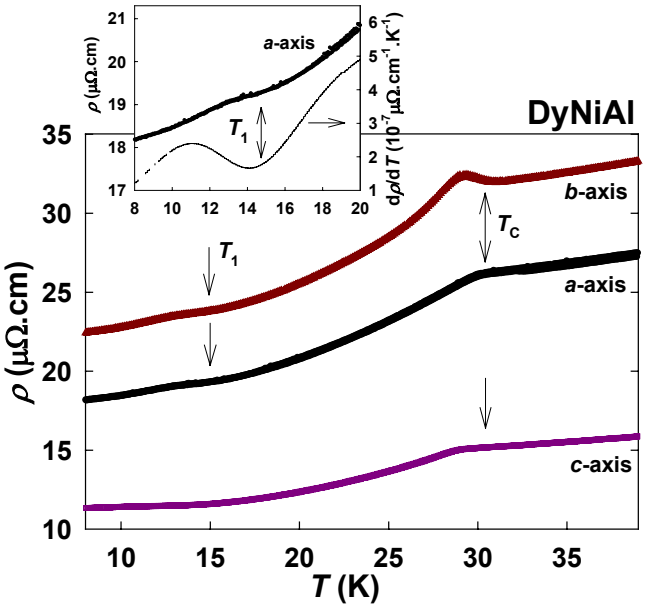

Figure 5.21: Temperature dependence of the resistivity of the DyNiAl crystal measured along individual axes at various temperatures. The detail shows the first derivative around the lower transition at 15 K. The arrows indicate the phase transitions.

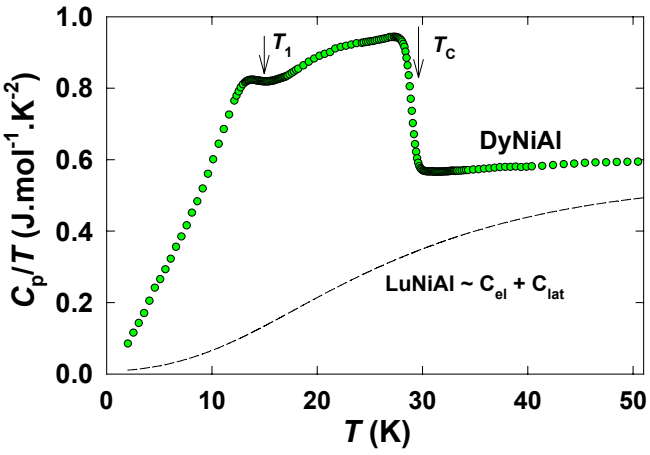

Figure 5.22: Temperature dependence of specific heat of the DyNiAl single crystal. The dashed line represents the heat capacity of the LuNiAl as the first approximation of the nonmagnetic contributions.

The phase transitions are reflected also on the resistivity measurements (Figure 5.21). The transition at T_1 is more visible on data measured along *a* and *b* axes, whereas for the current along the *c* axis it is not observed. The relatively high ρ_0 value is a common feature for these *RTX* compounds.

The specific heat data show well-pronounced anomalies at T_C and T_1. Taking the LuNiAl data [71,72] as a first approximation of the nonmagnetic (i.e. electronic and lattice) contribution in DyNiAl (see Figure 5.22), we get the magnetic entropy of 23.4 J.mol^{-1}K^{-1}, in good agreement with value of Rln(16) expected for the Dy^{3+} ion. The entropy at T_C reaches $\approx$ 15 J.mol^{-1}K^{-1} $\approx$ Rln(6), indicating that probably three lowest crystal-field doublets are involved in the magnetic ordering.

Neutron diffraction

The neutron diffraction experiment in zero magnetic fields (ILL Grenoble-D15) showed that magnetic intensities on the positions of nuclear reflections develop below T_C, then they increase by cooling down to T_1 and stay almost constant below T_1 (Figure 5.23), in agreement with powder data [44,45]. Additional reflections described by $\boldsymbol{k}$ = (½ 0 ½) propagation vector appear below T_1. In the hexagonal symmetry of DyNiAl and for this $\boldsymbol{k}$, three magnetic domains exist. We did not observe any significant differences between intensities of magnetic reflections corresponding to different domains (but from the same set). It means that all three magnetic domains are (almost) equally populated.

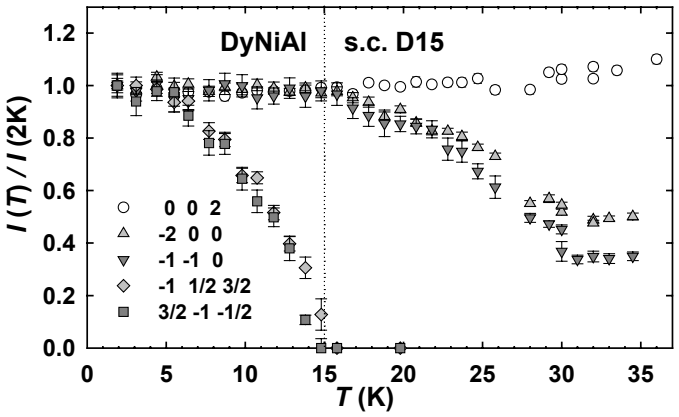

Figure 5.23: Temperature dependence of intensities of selected reflections in DyNiAl.

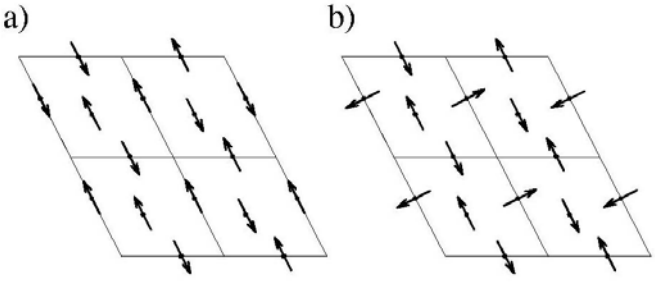

Figure 5.24: Two possible arrangements of the AF component in DyNiAl. Our results favor the a) arrangement.

To determine the magnetic structure at 2 K, intensities of reflections described by (0 0 0) or (½ 0 ½) p.v. were measured. The first set of reflections corresponds clearly to the F ordering of the *c*-component of the Dy magnetic moments. Moments on all the

three Dy-sites have the same orientation and magnitude $\mu_F = 7.1(1)\ \mu_B$, our refinement gives the agreement factor of $R_{WABS} = 6.2\%$. The refinement of the AF part ($\boldsymbol{k} = (½\ 0\ ½)$) favors clearly moment arrangement within the basal plane. The best agreement factor is obtained for structure shown in Figure 5.24a ($R_{WABS} = 10.0\%$). The AF components μ_{AF} on all the Dy-sites are parallel but that one on $(0,X_{Dy},½)$ position propagates with $\boldsymbol{k'} = (0\ ½\ ½)$ that is, in the hexagonal symmetry, equivalent vector to $(½\ 0\ ½)$. It is the same magnetic structure as in HoNiAl [73]. The AF component reaches $\mu_{AF} = 4.2(1)\ \mu_B$, resulting in the total Dy moment $\boldsymbol{\mu} = \boldsymbol{\mu}_{AF} + \boldsymbol{\mu}_F = 8.2(2)\ \mu_B$. All other magnetic structures, including that proposed from powder neutron data [44], give considerably worse agreement ($R_{WABS} = 17\%$ for structure shown in Figure 5.24b – second best result). Contrary to 7.2 μ_B derived from powder neutron data [44], the value of 8.2 μ_B is in agreement with our magnetization measurements and Mössbauer data [2]. However, Mössbauer data indicate two magnetically different Dy-sites, while we do not observe such indications. We cannot exclude sample-dependent results as revealed also for the HoNiAl [73].

While μ_F is almost constant below T_1, μ_{AF} increases when cooling down below T_1, leading to an increasing angle between the Dy magnetic moment and the *c*-axis (≈ 30° at 2 K). The lower value of the total moment in comparison to the free-ion value of 10 μ_B can be caused by the crystal field. Other possibility is

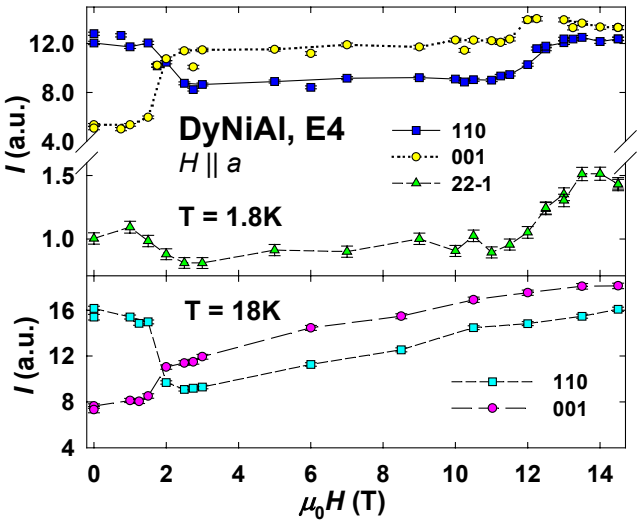

Figure 5.25: The field dependence of selected (*hhl*) reflections at the lowest temperature and at the temperature between T_C and T_1.

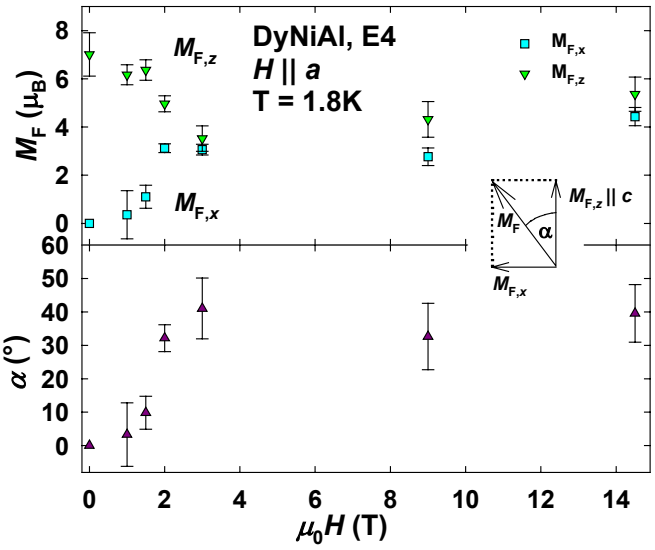

Figure 5.26: The field dependence of the ferromagnetic moment components $M_{F,x}$ and $M_{F,z}$ at 1.8 K. Also the angle between the resulting F component direction and the *c*-axis (α) is calculated.

fluctuation of the magnetic moment. In such case, high magnetic field can partly stabilize the fluctuation as really seen on magnetization data.

The results were obtained assuming that moments on all the Dy sites have the same magnitude. Allowing different magnitudes does not lead to any substantial improvement of our fits. Summary of the magnetic-structures parameters in zero magnetic field are given in the Table 5.6.

The neutron diffraction experiment under high magnetic fields (HMI Berlin-E4) applied in the $H \parallel a$ and the $H \parallel b$ configurations at 2 K confirmed that one field-induced transition occurs around $H_{C1} \approx 1.5$ T in both cases and the second one appears around $H_{C2} \approx 11\text{-}13$ T for $H \parallel a$ in agreement with magnetization measurements. The $H_{C2} \approx 22$ T in the $H \parallel b$ arrangement could not be reached.

In the $H \parallel a$ configuration, both transitions at H_{C1} and H_{C2} are seen in the field dependencies of diffraction intensities at 1.8 K (see Figure 5.25). At 18 K, the H_{C2} transition disappears and only gradual increase of the intensities is observed. This is in agreement with the F ordering in this temperature region. The geometry of the magnet and the sample orientation restricted us to measure only few reflections of the (*h h l*)-type (especially all reflections with $\boldsymbol{k} = (½\ 0\ ½)$ were shielded by the coils). The limited number of reflections did not allow us to check the domain population. We refined the ferromagnetic component assuming equal domain population (Figure 5.26). The magnitudes of the F component at 1.8 K are: μ_F (0T) = 7.0(9)μ_B and μ_F (14.5T) = 6.7(1.0)μ_B. This result is in agreement with the results in zero field (ILL), what confirms roughly our assumption about the domain population. Surprisingly, the orientation of the F component in fields above 13 T are not yet fully oriented along the applied magnetic field – the angle with the field is approximately 40° (see Figure 5.26). The increase of both (110) and (001) reflection above 12 T can be caused by either stabilization of the magnetic moment fluctuation by the magnetic field or reorientation of the AF component and adding its magnitude to the F part. Unfortunately, the study of AF component was not possible at this experimental arrangement.

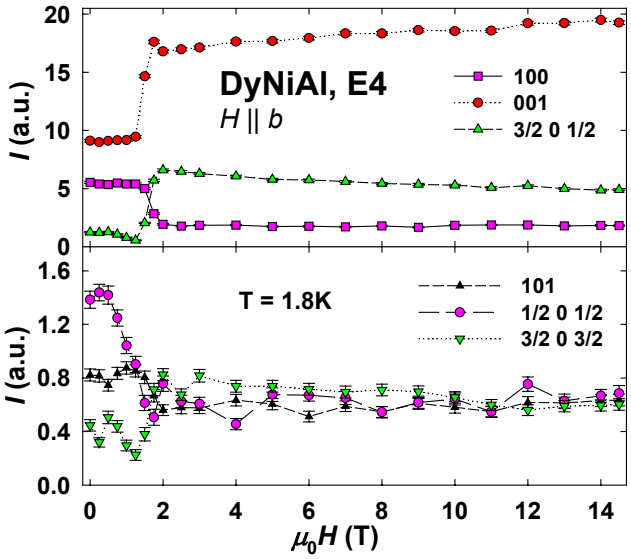

Figure 5.27: The field dependence of selected (*h*0*l*) reflections at the lowest temperature and at 18 K for the *H*||*b* configuration.

The data measured at $T = 18$ K present roughly equal increase of (110) and (001) reflections above 2 T. Thus, the absolute value of the moment increases whereas the angle to the *c*-axis remains almost unchanged.

In the $H \parallel b$ configuration, the appearance of another magnetic structure above ~1.5 T is indicated (see Figure 5.27), although the AF p.v. remains unchanged. Of course, we cannot exclude new component described by another p.v. The experimental set-up did not allow any efficient search in the reciprocal space. The (½ 0 ½) propagation does not vanish up to 14.5 T. The low- and the high-field magnetic structures differ in the direction of magnetic moments only. We could not reach the transition at H_{C2} that was observed around 22 T on the magnetization data in [69].

Table 5.6: Summary of parameters of the magnetic structures in DyNiAl.

T (K)	X_{Dy}	X_{Al}	μ_F (μ_B)	μ_{AF} (μ_B)	R_{WABS}(%)
40	0.5824(4)	0.235(2)	—	—	6.9
2	0.5824 !	0.235 !	7.1(1) $\parallel c$	4.2(1) $\perp c$	6.2^{F} / 10.0^{AF}

5.2.3 $DyNi_{1-x}Cu_xAl$

Paramagnetic region

In the paramagnetic region, the temperature dependencies of susceptibility in all studied compounds follow the modified Curie-Weiss law:

$$\chi = \frac{M}{H} = \frac{N_A \mu_0 \mu_B^2 \mu_{eff}^2}{3k_B(T-\theta_p)} + \chi_0 = \frac{C}{(T-\theta_p)} + \chi_0 \ . \qquad (5.2a)$$

The fits on the measured data lead to values of the effective moments μ_{eff} that are close to the Dy^{3+} free-ion value of 10.65 μ_B (Table 5.7). Paramagnetic Curie temperatures θ_p are positive in all cases, indicating major role of ferromagnetic interactions. The value of χ_0 was found to be of the order of 10^{-9} m^3/mol in all cases, comparable to the values of temperature independent susceptibility of YCuAl and LuCuAl [48].

$x = 0.1$ and 0.2

The low-temperature magnetization data of the compound with $x = 0.1$ show very similar behavior to parent DyNiAl with ferromagnetic ordering at $T_{ord} = 25$ K and antiferromagnetic order below $T_1 = 13$ K (see Figures 5.28a and 5.29a). Magnetization curves measured at temperatures below T_1 exhibit a field-induced phase transition around 2 T, most probably corresponding to the rotation of the antiferromagnetic component – that we expect to be located within the hexagonal basal plane similar to the arrangement in DyNiAl – since this transition is not seen above T_1 and one can observe only ferromagnetic character of the magnetization curve at 15 K, i.e. above T_1.

The microscopic study of the magnetic structure also showed that behavior of $DyNi_{0.9}Cu_{0.1}Al$ is similar to that one found in DyNiAl. This compound orders ferromagnetically with Dy moments parallel to the crystallographic *c*-axis (F || *c*) below T_C. Additional antiferromagnetic component (described by the propagation vector (½ 0 ½)) arranged within the basal plane (AF ⊥ *c*) adds to the ferromagnetic component below T_1 (see Figure 5.28a). Nevertheless, the exact arrangement of the AF component could not be determined due to very low intensities of the corresponding reflections (see Figure 5.30).

The sample with $x = 0.2$ is basically different – transition of antiferromagnetic type occurs already at T_{ord} ($T_N = 21$ K) – as seen in the temperature dependence of magnetization (see Figure 5.28b). Also the magnetization curve at 16 K, i.e. above T_1,

exhibits antiferromagnetic behavior (see Figure 5.29b,c). Ferromagnetic transition then probably onsets below T_1 = 11.5 K.

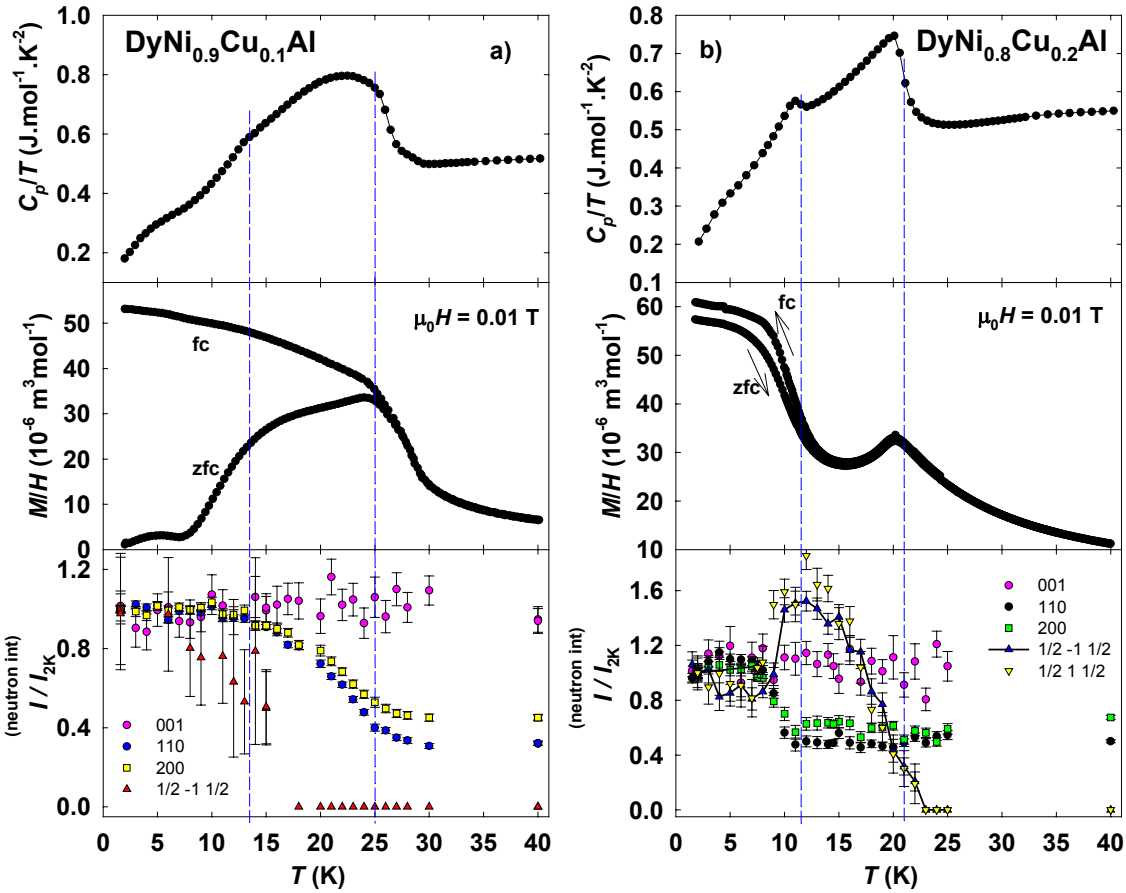

Figure 5.28: Temperature dependence of the heat capacity, DC-magnetization under field of 0.01 T and intensities of selected reflections measured by powder neutron diffraction for the $DyNi_{0.9}Cu_{0.1}Al$ and $DyNi_{0.8}Cu_{0.2}Al$ compounds. The vertical dashed lines point the temperatures of phase transitions as derived from the heat capacity.

The neutron-diffraction data confirm the stating of opposite sequence of the ordering types with respect to temperature in comparison to the $DyNi_{0.9}Cu_{0.1}Al$ compound. The antiferromagnetic reflections with propagation vector (½ 0 ½) start to appear around 22 K and the ferromagnetic intensities increase at lower temperatures around 11 K, as it can be seen on the Figure 5.28b. The magnetic moments above T_1 are oriented along the hexagonal *c*-axis and magnetic moments on the position (0, X_{Dy}, ½) are frustrated leading to almost zero magnitude. The magnetic structure is then similar to the high-temperature structure ($T_1 \leq T \leq T_{ord}$) of TbNiAl [52,67] (R_{mag} = 20%). Any other fit – especially with moments arrangement away from the *c*-axis direction brings rather worse fit. At 1.6 K the magnetic structure is similar to that one in DyNiAl – the AF component lies in the basal plane and the F component then appears along the *c*-axis.

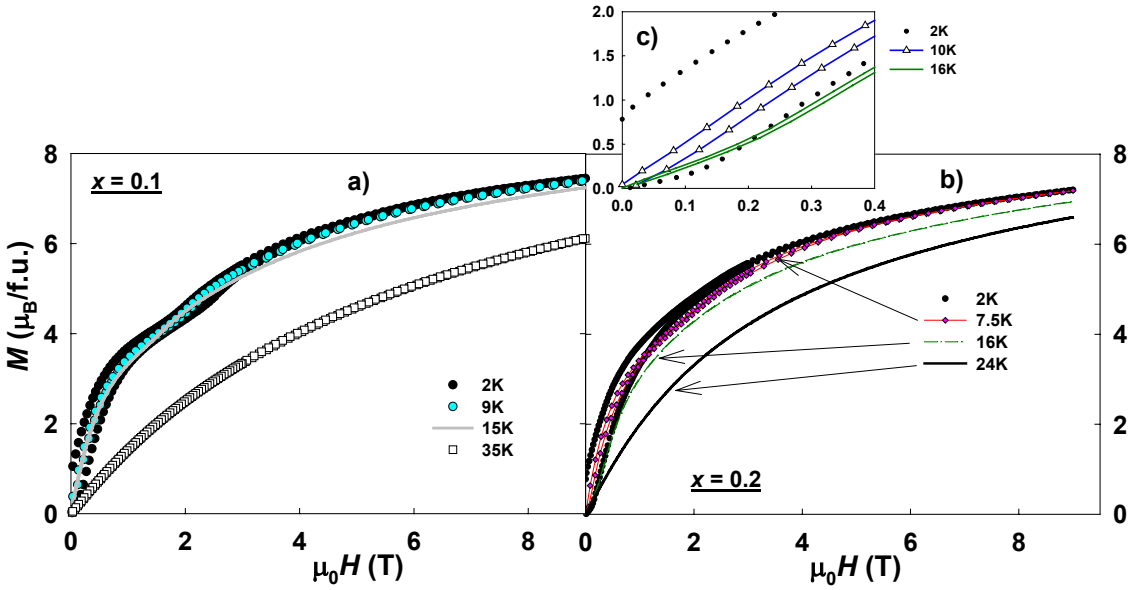

Figure 5.29: The magnetization curves of the $DyNi_{0.9}Cu_{0.1}Al$ and $DyNi_{0.8}Cu_{0.2}Al$ compounds. Opposite sequence of the F and AF order can be visible also on these data.

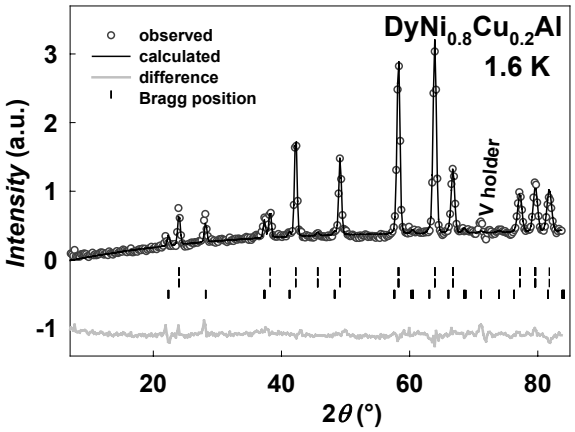

Figure 5.31: The refined neutron pattern of the $DyNi_{0.8}Cu_{0.2}Al$ compound in the magnetically ordered state.

The agreement factors for the AF component for the compounds with $x = 0.1$ and 0.2 as displayed in the Table 5.7 are enhanced due to low intensities of the AF reflections at 1.6 K (see Figure 5.30). For the same reason we could not refine the exact magnetic structure of AF components within the basal plane. We can only state that they lie in the basal plane. Fit with the antiferromagnetic components along the *c*-axis leads to

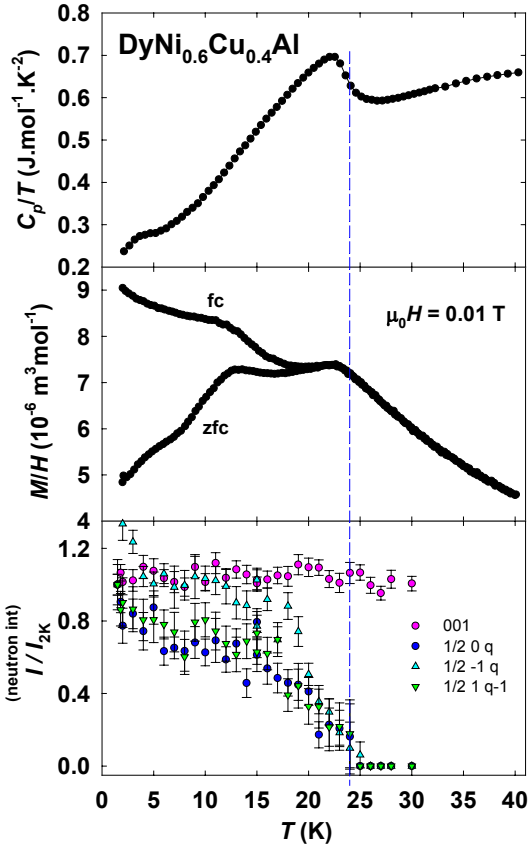

Figure 5.32: Temperature dependence of the heat capacity, DC-magnetization under field of 0.01 T and intensities of selected reflections measured by powder neutron diffraction for the $DyNi_{0.6}Cu_{0.4}Al$ compounds. The vertical dashed line points the temperature of phase transition as derived from the heat capacity.

worse agreement, especially the calculated intensity on the position of the (½ 0 ½) and (½ 1 ½) reflections would be zero in such case, while the measured one is clearly present. An example of the magnetic-structure fit is displayed on the Figure 5.31.

$$0.3 \leq x \leq 0.5$$

The low-temperature dependencies of magnetization for samples with $x = 0.3$-0.5 exhibit all similar behavior (as an example see Figure 5.32). These data show antiferromagnetic transition at T_{ord} and possible another phase-to-phase transition at lower temperatures but this anomaly was not confirmed by any of other used techniques (heat capacity, neutron diffraction). Magnetization curves indicate consequent suppression of ferromagnetic component from $x = 0.1$ to 0.4 (Figure 5.33). Weakening of ferromagnetism in this concentration region is corroborated by the minimum of θ_p (see Table 5.7). The anomaly visible on the heat capacity data in $DyNi_{0.6}Cu_{0.4}Al$ around 5 K is probably caused by the impurity phase.

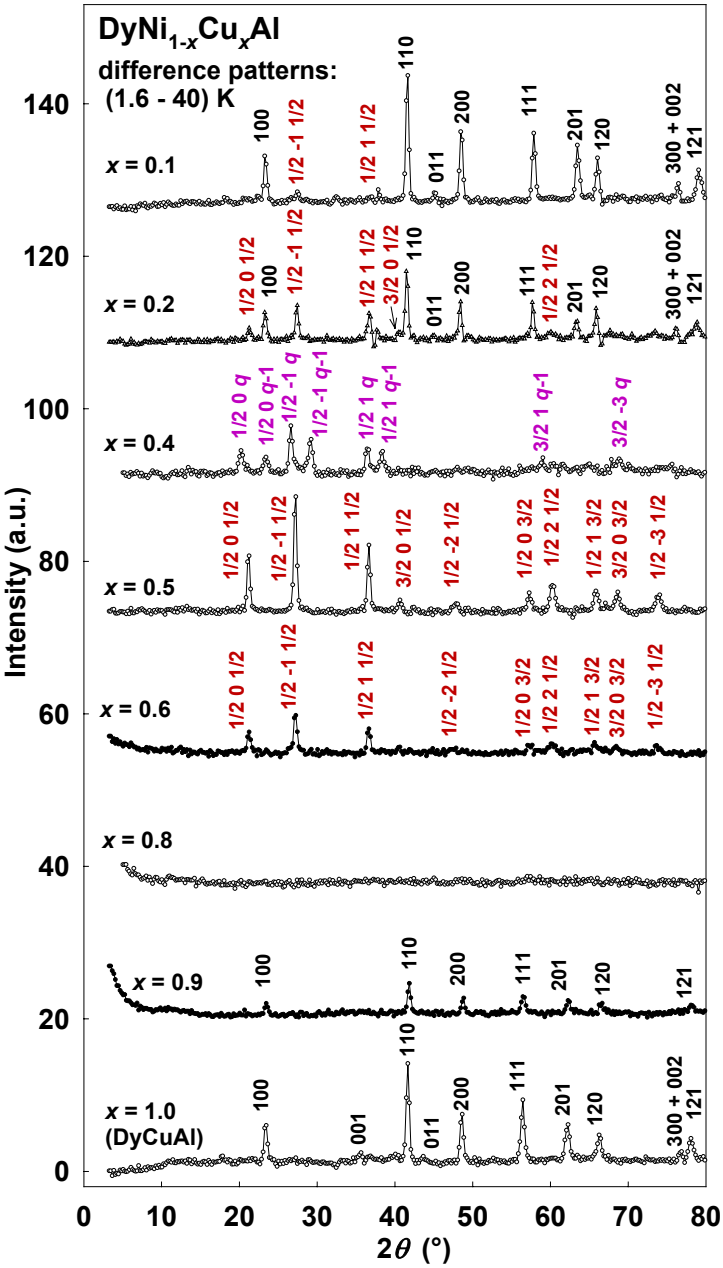

Figure 5.30: Difference neutron patterns between the ordered state (or lowest studied temperature) and the paramagnetic state of $DyNi_{1-x}Cu_xAl$ compounds. The data are shifted for better view.

The neutron diffraction pattern of the $DyNi_{0.7}Cu_{0.3}Al$ compound also showed an antiferromagnetic order but due to weakness of the reflections and also due to low quality of this one sample, that was caused probably by vicinity of the structural transition and possible existence of two different crystal phases at low temperature in

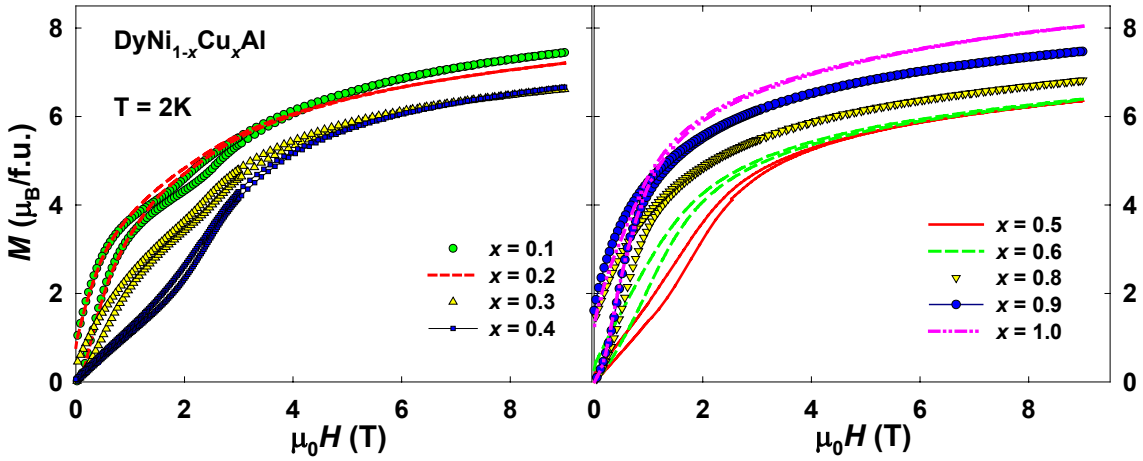

Figure 5.33: Comparison of magnetization curves of all studied $DyNi_{1-x}Cu_xAl$ compounds at T = 2 K. The strongest AF character can be visible for samples around x = 0.4 and 0.5.

this compound (different *a,c* parameters due to forbidden *c/a* ratio; see section 5.1 Results – Crystal structure), we were not able to determine the magnetic structure in more detail and we state just the AF order in the Table 5.7 without any other detail of magnetic structure. The $DyNi_{0.6}Cu_{0.4}Al$ compound exhibits the AF incommensurate order with the propagation vector $\boldsymbol{k'} = (½\ 0\ q)$, where q = 0.448, while the sample with $x = 0.5$ orders again with the commensurate propagation (½ 0 ½) and moments adjusted within the basal plane (see Figure 5.30). Again, we could not refine the exact magnetic structure of AF components within the basal plane due to low intensities of the AF reflections.

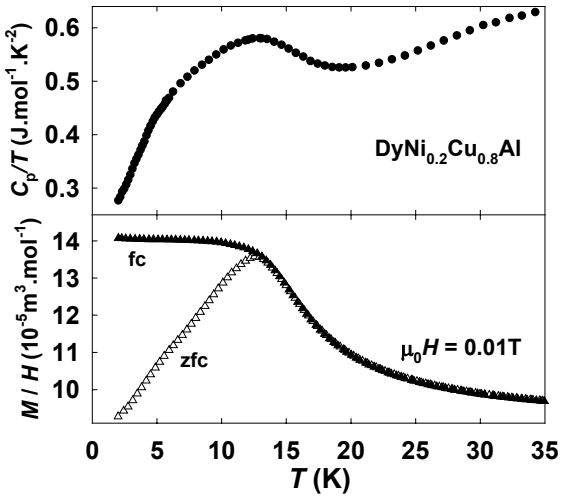

Figure 5.34: Temperature dependence of DC-magnetization and heat capacity for the $DyNi_{0.2}Cu_{0.8}Al$ compound.

x = 0.6 and 0.8

The samples with $x = 0.6$ and 0.8 exhibit rather broader maximum in *M/H* vs. *T* dependence and also very broad anomaly in the temperature dependence of

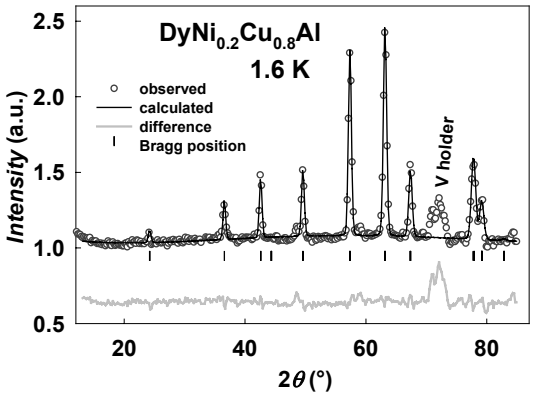

Figure 5.35: The neutron diffraction pattern of the $DyNi_{0.2}Cu_{0.8}Al$ compound can be fitted just with the crystal structure at 1.6 K.

heat capacity (see Figure 5.34) which can indicate loss of long-range magnetic order (see below).

The neutron diffraction found an antiferromagnetic order in the $DyNi_{0.4}Cu_{0.6}Al$ compound with quite weak magnetic reflections and reduced magnetic moments ($\mu_{AF} = 4.1(2)\ \mu_B$) and with signs of short-range correlations (enhanced intensity at low angles; see Figure 5.30). The magnetic moments propagate with commensurate $\boldsymbol{k} = (½\ 0\ ½)$ and the moments are adjusted within the basal plane. When spanning the parameter x from 0.5 to 0.8, the ordered magnetic moment is getting smaller and the long-range magnetic order becomes weaker resulting in the total loss of the long-range order for $x = 0.8$. This can be observed on the difference pattern between the lowest studied temperature of 1.6 K and paramagnetic state (40 K; see Figure 5.30). The difference is practically zero except for enhanced intensity at low angles what indicates short-range correlations around the (0 0 0) reflection. The low-temperature pattern of $DyNi_{0.2}Cu_{0.8}Al$ at $T = 1.6$ K can then be described by the nuclear structure only (with $R_{Bragg} = 5.7\%$; see Figure 5.35).

Table 5.7: Summary of magnetic properties for the $DyNi_{1-x}Cu_xAl$ series. The results displayed for the compound with $x = 0.0$ (DyNiAl) were obtained from the DyNiAl-single crystal measurements. The magnetic structure of the $DyNi_{0.7}Cu_{0.3}Al$ compound was not determined due to low-quality diffraction pattern at 1.6 K. The parameters obtained from the bulk data of DyCuAl were taken from [48], whereas the parameters of the magnetic structure were obtained from the results of the powder neutron diffraction experiment at 1.8 K. The signs of short-range order could be visible on samples with $0.6 \le x \le 0.9$.

x	μ_{eff} (μ_B)	θ_p (K)	T_{ord} (K)	T_1 (K)	μ_{Dy} (μ_B)	p.v.	type	R_{mag} (%)
0.0	10.65	11 $^{H\|\|b}$ 46 $^{H\|\|c}$	30.0 (0.5)	15.0 (0.5)	7.1 (1) 4.2 (1)	(0 0 0) (½ 0 ½)	F ∥ c AF ⊥ c	6.2 10.0
0.1	10.76 (1)	16.6 (2)	25.0 (1.0)	13.0 (0.8)	7.1 (3) 1.7 (4)	(0 0 0) (½ 0 ½)	F ∥ c AF ⊥ c	5.4 66
0.2	10.75 (1)	13.3 (2)	21.0 (0.5)	11.5 (0.2)	5.1 (3) 3.0 (3)	(0 0 0) (½ 0 ½)	F ∥ c AF ⊥ c	5.0 42
0.3	10.72 (2)	10.2 (3)	19.0 (0.5)	14.5 (0.5)	?	?	AF ?	—
0.4	11.08 (1)	6.5 (2)	24.0 (0.5)	—	4.7 (2)	(½ 0 0.448)	AF ⊥ c	18
0.5	10.96 (2)	7.1 (3)	20.5 (0.5)	—	5.7 (5)	(½ 0 ½)	AF ⊥ c	10
0.6	11.02 (2)	6.8 (2)	20.0 (1.0)	—	4.1 (2)	(½ 0 ½) & SRO	AF ⊥ c	13
0.8	11.06 (2)	11.3 (2)	—	—		SRO		—
0.9	10.87 (1)	18.2 (2)	18.5 (1.0)	—	3.8 (6)	(0 0 0)	F ∥ c	3.7
1.0	10.65[48]	25.9[48]	28[48]	—	5.8 (4)	(0 0 0)	F ∥ c	7.5

x = 0.9 and DyCuAl

Bulk data for the compounds with $x \geq 0.9$ exhibit already more F-like *M/H* vs. *T* dependencies, similar to DyCuAl [48] (and so also does the sample with $x = 0.8$, but in this sample the long-range ferromagnetic order was not found). Strengthening of the ferromagnetic component from $x = 0.6$ to 1.0 can be deduced from magnetization curves (see Figure 5.33). There is a small bend on magnetization curves visible in smaller fields (~0.2 T), which was also observed earlier in DyCuAl [48] what could be in accordance with expected antiferromagnetic component in the low-temperature phase (in analogy with DyNiAl) but the antiferromagnetic component was not confirmed by the microscopic method (neutron diffraction).

Using the neutron diffraction the magnetic structures in $DyNi_{0.1}Cu_{0.9}Al$ and DyCuAl compounds were found to be simple ferromagnetic with moments aligned along the *c*-axes and with magnitudes $\mu_{Dy} = 3.2(1.0)\ \mu_B$ and $5.4(8)\ \mu_B$. for $x = 0.9$ and 1.0 (DyCuAl), respectively. The magnetic reflections – and thus the moments – are getting stronger with increasing *x* (see Figure 5.30). Simple ferromagnetic order in DyCuAl is in contradiction with the bulk data that indicated similar behavior to DyNiAl, i.e. with two magnetic phases and the AF component in the ground state. Strong dependence of magnetic properties on the sample quality could be an explanation and was discussed e.g. for isostructural HoNiAl [73].

6. Discussion

6.1 Crystal structure

The most interesting result of our crystal-structure investigations is the observation of the "forbidden *c/a*" region. When approaching the forbidden *c/a* values by varying the composition or temperature, the structural step is observed (see Figures 6.1 and 6.2). A common property of the studied compounds showing such a step in the lattice-parameters is that the discontinuity is not connected with a deviation from the linear evolution of the volume. The step is probably caused by different atomic-bonding forces within basal planes and between the planes. This may cause an abrupt change in *c*/*a* ratio as it is observed. More generally, in compounds crystallizing in ZrNiAl-type structure there is probably "forbidden" *c/a* ratio around $c/a \approx 0.565\sim0.573$ because, around this value, the structural discontinuity happens in several series (Tb-, Er- and Dy-based). The step can be observed also when going through the *R*NiAl [2], *R*PdAl [28] and *R*CuAl [1] compounds at room temperature (see

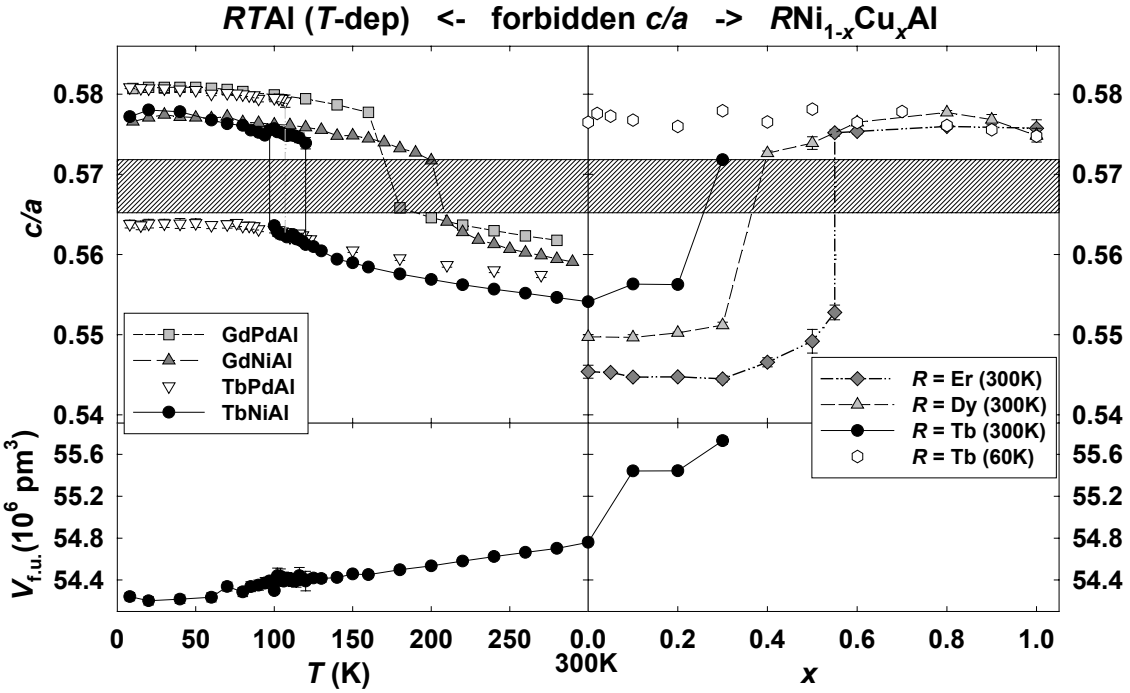

Figure 6.1: Demonstration of the forbidden *c/a* ratio values for *RT*Al compounds – realized either by substitution or by variation of the temperature. The example of monotonous evolution of the volume of the Tb-based compounds is displayed to demonstrate contradiction between the behavior of *c/a* and the volume. The data for the GdPdAl and GdNiAl were estimated from the figures in Refs [65,63].

Figure 6.2). In several other *RTX* compounds, this value of the *c/a* ratio is absent in the evolution of the lattice with temperature as well (e.g. TbNiAl, TbPdAl, GdPdAl [65,66],

GdNiAl [63,64]) as can be seen in the Figure 6.1. The two exceptions – $TbPd_{1-x}Ni_xAl$ and $Ce_{1-x}Y_xPdAl$ – will be discussed below.

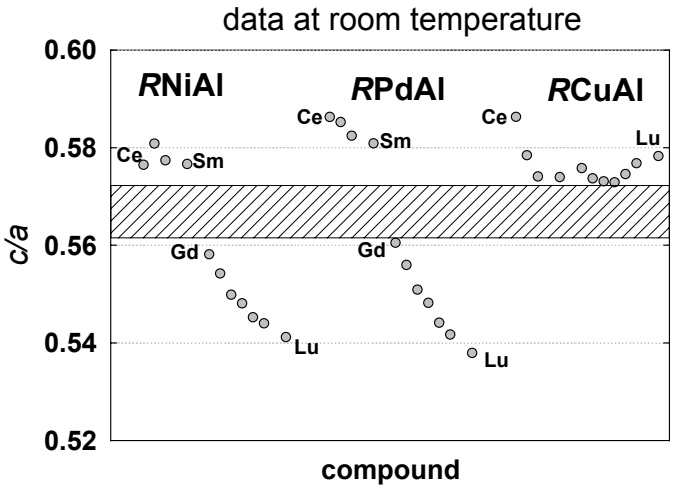

Figure 6.2: Development of the *c/a* ratio in the *R*NiAl [2], *R*PdAl [28] and *R*CuAl [1] series. Individual points in each series correspond to different rare-earth element in the following order: Ce, Pr, Nd, Sm, Gd, Tb, Dy, Ho, Er, Tm, Lu. Data for compounds with *R* = Eu are not available.

The Figure 6.3 displays a general property of the $RNi_{1-x}Cu_xAl$ series concerning the structural discontinuity. We used the data obtained in this work together with results of other authors in order to get a systematic boundary between the compounds with "high *c/a*" and the compounds with "low *c/a*" ratio (according to the notation introduced in the Section 5.1 Crystal structure). The data in Figure 6.3 were taken from the following sources:

-SmNiAl – Ref [63],
-SmCuAl and GdCuAl – Ref [48],
-GdNiAl – Ref [63],
-$TbNi_{1-x}Cu_xAl$ – Ref [62] and our present results,
-DyNiAl (Tdep) – Ref [74],
-$DyNi_{1-x}Cu_xAl$ – our present results,
-HoNiAl – Ref [73],
-$ErNi_{1-x}Cu_xAl$ – our present results.

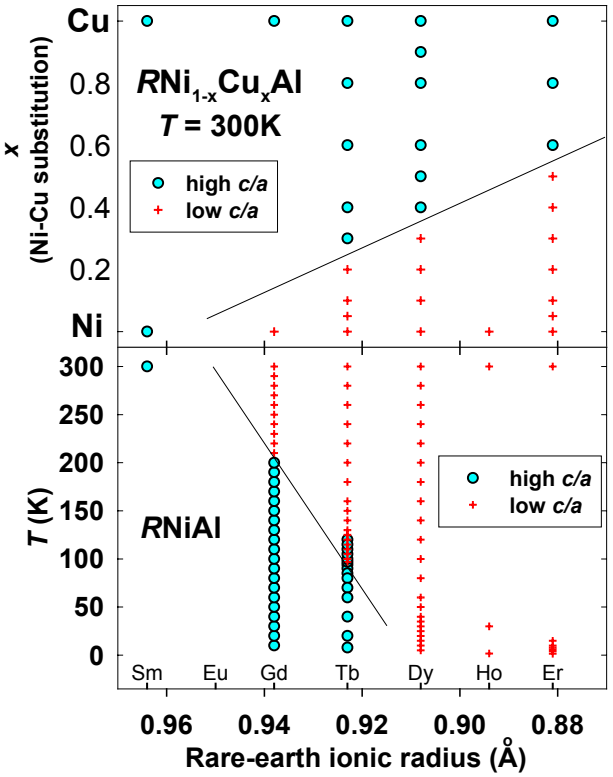

Figure 6.3: Systematic evolution of the boundary between "high-*c/a*" and "low-*c/a*" $RNi_{1-x}Cu_xAl$ compounds with respect to composition and temperature.

An interesting feature that should be pointed out from this figure is the fact that the structural discontinuity is not a direct question of volume change – i.e. one cannot decide whether the boundary will be reached by increasing or decreasing the volume. To explain this statement on an example we focus on the compounds with R = Tb. When moving from TbCuAl to TbNiAl (substitution Ni instead for Cu – i.e. moving from x = 1.0 down to 0.0; see

Figures 6.1 and 6.3) at room temperature, the structural discontinuity occurs between $x = 0.3$ and 0.2. At this point, the *c/a* ratio changes from "high *c/a*" value ($c/a_{0.3} \approx 0.572$) to "low *c/a*" one ($c/a_{0.2} \approx 0.556$) and the volume change is negative (the volume decreases – see Figure 5.4). On the other hand, when cooling the TbNiAl compound down (i.e. further decreasing of the volume – according the Figure 6.1), the *c/a* ratio exhibits a sudden change from "low *c/a*" to "high *c/a*" value around approximately $T = 110$ K ($c/a_{125\mathrm{K}} \approx 0.561$; $c/a_{94\mathrm{K}} \approx 0.575$) while the volume still decreases (Figure 6.1). As it can be seen from Figures 5.2 and 5.3, the structural discontinuity does not affect the linearity of the volume evolution in other series as well.

Hydrostatic pressure is another parameter than can be varied to cross the critical values of the *c/a* ratio. Recently, under a hydrostatic pressure of 0.95 GPa, a first-order transition has been observed in the temperature dependence of the electrical of $ErNi_{0.2}Cu_{0.8}Al$ [75]. Although the crystal structure was not studied directly by microscopic methods under the pressure, our suggestion that this change of resistivity is connected with a change in the crystal structure is supported by the fact that the resistivity anomaly is reversible and that the composition of the $ErNi_{0.2}Cu_{0.8}Al$ sample is close to the critical region where the structural step happens in the $ErNi_{1-x}Cu_xAl$ series. Thus, it is probable that the structural discontinuity shifts along the *x*-scale due to hydrostatic pressure to higher values of the Cu-content.

In the case of the $Ce_{1-x}Y_xPdAl$ and $TbPd_{1-x}Ni_xAl$ compounds the lattice parameters fall into the estimated forbidden *c/a*-shell. Here, the difference with the other studied compounds is the substitution of one element by another one that is quite different by volume from the original one (Ni-Pd, Ce-Y). The Ni-Pd (Ce-Y) disorder can play an important role and lead to breaking the rule of forbidden *c/a* or the rule can be a bit changed – e.g. the forbidden shell might be shifted to different values – and these compounds can be considered as exceptions from the discovered rule. The idea of shifted forbidden *c/a* range supports the fact that in these compounds a transition was still observed wit several changes – in the case of $Ce_{1-x}Y_xPdAl$ compounds the coexistence of two phases is present as preferred state instead of single phase with another *a,c* parameters, what makes the step-like character of the evolution of the lattice. In the $TbPd_{1-x}Ni_xAl$ compounds, the samples crossing the region of forbidden *c/a* values exhibit transition of higher order (see Figure 5.12). To confirm or discard possible Ni-Pd disorder in the $TbPd_{1-x}Ni_xAl$ compounds, neutron-diffraction experiment at ILL is already scheduled.

6.2 Magnetism

Measurements of magnetic properties in the quasi-ternary $R\mathrm{Ni}_{1-x}\mathrm{Cu}_x\mathrm{Al}$ series showed that the conversion between the *R*NiAl and *R*CuAl compounds is rather complex. Already small Cu-substitution leads to change in character of magnetic behavior – even in the case of the Dy-based series where almost no change was expected. In both studied series the magnetic evolution goes through complicated magnetic structures to final ferromagnetic order in *R*CuAl. The fact that the anisotropy begins to change already for low Cu-substitution in $\mathrm{ErNi}_{1-x}\mathrm{Cu}_x\mathrm{Al}$ (and small lattice change) indicates that the anisotropy is rather weak in ErNiAl. This conclusion is corroborated by magnetization data obtained on an ErNiAl single-crystal [71].

In both series studied in this work and in former study on the Tb(Ni,Cu)Al system, a large concentration scale ($0.6 \leq x \leq 0.9$) is characterized with presence of short-range correlations on the account of the long-range order. Especially the samples with $x = 0.8$ are characterized by no long-range magnetic order at all. This is well seen also by the heat-capacity data for the Er-based series (see Figure 3.3), where the anomaly becomes very broad for $x = 0.8$ and is centred at a temperature higher than the temperature of M vs. T maximum.

Since the magnetic long-range order is lost in all studied systems at the same Cu-concentration, the number of 3*d* electrons in the Ni-Cu sublattice seems to be the crucial parameter here, and neither the structural anomaly nor the rare-earth elements play considerable role in this effect. There is no unambiguous explanation up to now. Let us discuss some possible mechanisms. Already the rather low magnetic temperatures of the $R\mathrm{Ni}_{1-x}\mathrm{Cu}_x\mathrm{Al}$ compounds indicate that the indirect RKKY-type exchange interactions are mainly responsible for magnetic order in these materials. A question arises how the itinerant 3*d* electrons brought in the system by Ni enter in the exchange interaction game. One scenario proposed by Ehlers et al. [3] based on work of Campbell [11] considers an exchange interaction mediated by the transition-metal free 3*d* electrons competing with the RKKY interaction. Result of this competition may be the frustrated state for certain composition of the (Ni,Cu) sublattice. Another approach may be to include the itinerant 3*d* electrons to the overall balance of conduction electrons mediating the *R*–*R* exchange interaction (in fact the RKKY-type).

Concerning the above-mentioned model proposed by Ehlers, the exchange interactions are mediated mainly by the Ni 3*d*-electrons below $x = 0.60$. Since in Cu-rich compounds there are almost no free Ni-states, the indirect coupling must be mediated by *s*-electrons. The change in coupling mechanism from *d*- to *s*-electron polarization takes place most probably in the range $x \in (0.6; 0.8)$. The Ni-magnetic states do not manifest themselves in any of these compounds. Its presence cannot be

proved by a neutron diffraction experiment due to too high difference in signals obtained from eventual Ni-moments (~ 0.1 μ_B) and from the rare-earth moments (~ 4-8 μ_B). Such estimation needs to perform a site-specific experiment what could be for example X-ray resonant magnetic scattering.

The magnitudes of the *R*-moments determined by different experimental techniques (neutron diffraction, magnetization – including measurements on DyNiAl single crystal, Mössbauer spectroscopy [2]) agree very well with each other. These moments are significantly smaller than the free-ion values. This can be caused mainly by the crystal-field effect. Also the frustration of the moments that occurs quite often in compounds with the hexagonal symmetry and triangular arrangement of the magnetic atoms (e.g. [76,77]) can be another factor. Third contributor is probably the competition of the exchange mechanisms as described above that cause decrease of magnitudes of the ordered moments around the critical region of substitution ($x = 0.8$). Reduced magnetic moments with respect to the free-ion values are observed in many compounds with this crystal structure – e.g. in TmPdIn [78], ErPtIn [79], TbPtIn [80], HoPtIn [81], ErPdIn [81], HoAuIn [82].

There is one more aspect of evolution of magnetic order with varying the composition of the (Ni,Cu) sublattice. The incommensurate (IC) propagation in Er-based system was found in range of $0.2 \leq x \leq 0.4$. In the Dy-based series, we found it in a quite narrower region (just the $DyNi_{0.6}Cu_{0.4}Al$ sample) and in the Tb-based compounds already no incommensurate propagation at all has been observed [3]. On the other hand, there is IC propagation in TmCuAl [50]. The IC propagation was also reported for compounds from the opposite end of the

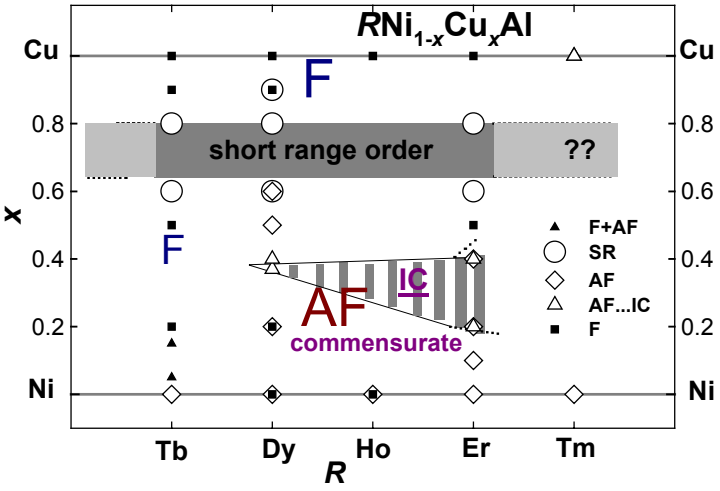

Figure 6.4: The enhanced tendency to incommensurate propagation with decreasing free *f*-electron states. The data for other than Dy- and Er-based series were taken from Refs: [3] - Tb, [44,48] - Ho, [1,50] - Tm. The remarks have following meaning:
-AF = antiferromagnetic order
-AF...IC = antiferromagnetic order with incommensurate propagation
-F+AF = coexistence of AF and F in sense of different parts of sample
-SR = signs of short-range order
-F = ferromagnetic order
If there are two marks on one position – e.g. for F and AF in $DyNi_{0.8}Cu_{0.2}Al$ sample – there are two coexisting components of the ordered moment (different from F + AF!).

lanthanide group, PrNiAl and NdNiAl [44]. One can see the tendency when spanning the lanthanide group in the periodic table of elements shown in Figure 6.4 suggesting that the incommensurate propagation is connected with the occupancy of the 4*f*-electron shell, i.e. it appears namely for compounds having *R*-element with either almost empty or almost full *f*-electron shell. Further observed tendency is the strengthening of antiferromagnetism when going from Tb- to Tm- compounds. Data shown in the Figure 6.4 corresponding to another than Dy- and Er-based series were taken from Refs.: [3]-Tb, [44,48]-Ho, [1,50]-Tm.

Moreover, we found out in our experiment that the parent compound DyCuAl does not exhibit the AF component like the DyNiAl what is in contradiction to presumption of similar behavior determined from bulk data [48]. Nevertheless, we cannot exclude the possibility of sample (or sample-quality) dependence of the results that could cause the discrepancy of our neutron-diffraction results made on the DyCuAl sample with that ones performed on different sample of the same compound by previous study [48].

6.3 Relation between structural and magnetic properties

In the case of Er-based series, the step-like change in lattice parameters could inspire an idea that the anisotropy would change suddenly just at the concentration where the step is observed, but the neutron diffraction reveals that the anisotropy change is not connected primarily with the lattice discontinuity. We observe a continuous gradual change instead, clearly demonstrated in Figure 5.16. The transition from AF to F and change of the magnetocrystalline anisotropy occur independently on structure discontinuity (the *c/a* step), that could have only minor influence e.g. on crystal-field parameters (see Figure 6.5). Recent study of crystal field discovered the change of the energy-levels evolution in the point of the structural transition within the $ErNi_{1-x}Cu_xAl$ series [72] – see Figure 6.5. Also in the Dy-based series the step observable within the Cu-concentration scale is not connected with any sudden change in magnetic properties.

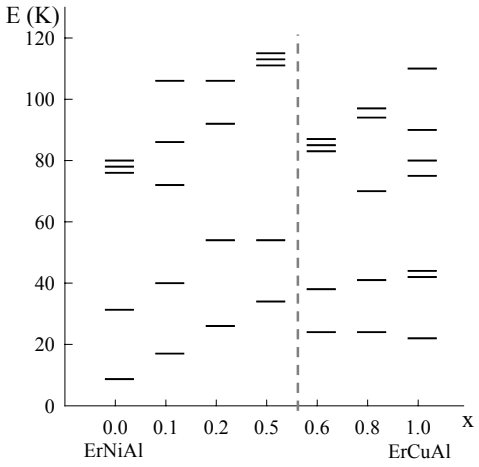

Figure 6.5: Lower part of the energy-level schemes in the $ErNi_{1-x}Cu_xAl$ series as derived from specific-heat data. Change in the tendency is visible between $x = 0.5$ and 0.6, where the structural change was found (see the gray dashed line). The figure is taken from Ref. [72].

The structural discontinuity seems then to be rather a consequence of geometrical properties and chemical-bonding forces, since this effect is present in both – the paramagnetic and ordered state. The shift of the *c*/*a* ratio through the lanthanide period in the periodic table is systematic with respect to rare-earth atomic radius, temperature and the transition-metal substitution.

A closer study of the energy levels using inelastic neutron scattering experiment is worthy to perform in order to investigate the structural discontinuity from point of view of microscopic method. The compounds exhibiting the step in temperature evolution are good candidates since there is no danger of different sample quality below- and above-the step.

7. Conclusions

We have studied two selected pseudoternary series with the formula $R\mathrm{Ni}_{1-x}\mathrm{Cu}_x\mathrm{Al}$ and with R = Er and Dy including a DyNiAl single crystal from point of view of magnetic behavior. Also a crystal-structure study was performed both above-mentioned series together with several other isostructural compounds selected on the basis of the discovered effect mentioned below.

In the studied $R\mathrm{Ni}_{1-x}\mathrm{Cu}_x\mathrm{Al}$ series (R = Er, Dy), a structural discontinuity in the evolution of the lattice parameters was found. A common property of the discontinuity is the absence of similar values of the *c/a* ratio of the lattice constants. A similar feature was also observed for other compounds (e.g. in the $\mathrm{TbNi}_{1-x}\mathrm{Cu}_x\mathrm{Al}$ series at room temperature and in the temperature evolution of the lattice parameters of TbNiAl, $\mathrm{TbNi}_{0.9}\mathrm{Cu}_{0.1}\mathrm{Al}$, $\mathrm{TbNi}_{0.8}\mathrm{Cu}_{0.2}\mathrm{Al}$, TbPdAl and $\mathrm{ErNi}_{0.45}\mathrm{Cu}_{0.55}\mathrm{Al}$) where similar *c/a* values were absent. A rule of "forbidden *c/a* values" for the *RT*Al compounds crystallizing the ZrNiAl structure was established and is corroborated by the results obtained by other authors. A systematic evolution of the boundary within the *x*-parameter for $R\mathrm{Ni}_{1-x}\mathrm{Cu}_x\mathrm{Al}$ compounds and within the temperature for *R*NiAl compounds was also found (see Figure 6.3). In our study, two exceptions were found that do not follow this rule – $\mathrm{Ce}_{1-x}\mathrm{Y}_x\mathrm{PdAl}$ and $\mathrm{TbPd}_{1-x}\mathrm{Ni}_x\mathrm{Al}$. These exceptions are discussed on the basis of substituted atoms with a too much different radial extent (Ce-Y, Pd-Ni).

In the magnetic study, the common property is the complex magnetic behavior of the substituted compounds, much more complicated than was expected on the basis of the behavior of the parent compounds. A common property of all studied compounds, including previous results on $\mathrm{TbNi}_{1-x}\mathrm{Cu}_x\mathrm{Al}$, is the loss of the long-range magnetic order in a similar Cu-concentration region (around x = 0.8), presumably due to competition of different exchange interactions. Another property that was found is the enhanced tendency to antiferromagnetic order and incommensurate propagation when going from Tb to Tm in the $R\mathrm{Ni}_{1-x}\mathrm{Cu}_x\mathrm{Al}$ series.

We have been seeking for a connection between the structural step and the evolution of magnetic behavior. However, no direct connection between the structural discontinuity and the changes in magnetic structure was found. We can conclude that mainly the number of *d*-electrons governs the development of magnetic properties within the $R\mathrm{Ni}_{1-x}\mathrm{Cu}_x\mathrm{Al}$ series.

A further study of the corresponding compounds by means of inelastic neutron scattering (determination of changes in the crystal-field energy levels) and local-probe methods like μSR is proposed for better understanding of the nature of the structural

discontinuity and of the compounds in the composition region where no long-range magnetic order was found. In the future, it is also worthy to perform a study of series with *R* from the group of light rare-earth elements, like Sm, Nd or Pr, to investigate the possible existence of aspects of the observed phenomena for a wider range of the rare-earth elements.

8. References

[1] N.C.Tuan, Magnetism in RNiAl compounds; doctoral thesis, Prague, 1992.

[2] P.Javorský, Magnetism in *R*CuAl and *R*NiAl compounds; doctoral thesis, Prague, 1997.

[3] G.Ehlers, D.Ahlert, C.Ritter, W.Miekeley, H.Maletta, Europhysics Letters, 37 (1997) 269.

[4] J.Prchal, Experimentální studium elektronových vlastností systému $RT_{1-x}T'_xAl$; master thesis, Prague, 2002.

[5] N.W.Ashcroft, N.D.Mermin, Solid State Physics, Saunders College, Philadelphia, 1976.

[6] Ch.Kittel, Úvod do fyziky pevných látek, Academia, Praha, 1985.

[7] J.Klíma, B.Velický, Kvantová mechanika I., II., MFF UK, Praha, 1992.

[8] M.T.Hutchings, Solid state physics, 16 (1964) 227.

[9] H.A.Kramers, Koninklijke Ned. Akad. Wetenschappen, B33 (1930) 959.

[10] H.A.Jahn, E.Teller, Proc. Roy. Soc., A161 (1937) 220.

[11] I.A.Campbell, J. Phys. F: Metal Phys., 2 (1972) L47.

[12] V.F.Sears, Neutron News, 3 (1992) 26.

[13] C.Stassis, H.W.Deckman, .N.Harmon, J.P.Desclaux, A.J.Freeman, Physical Review B, 15 (1977) 369.

[14] J.Rodriguez-Carvajal, Physica B, 192 (1993) 55.

[15] Neutron and Synchrotron Radiation for Condensed Matter Studies, Springer-Verlag, Berlin-Heidelberg, 1993.

[16] V.Valvoda, M.Polcarová, P.Lukáè, Základy strukturní analýzy, Karolinum, Praha, 1992.

[17] Stephen W.Lovesey, Theory of Neutron Scattering from Condensed Matter, Oxford University Press, 1987.

[18] H.M.Rietveld, Journal of Applied Crystallography, 2 (1969) 65.

[19] International Tables for X-ray Crystallography, International Union of Crystallography, Utrecht, 1968, pp. 157-200.

[20] V.Sechovský, L.Havela, in E.P.Wolfhart, K.H.J.Buschow (Eds.), Ferromagnetic Materials, North-Holland, 1988, p. 309.

[21] A.Szytuła, M.Kolenda, J.Leciejewicz, N.Stüsser, Journal of Magnetism and Magnetic Materials, 164 (1996) 377.

[22] A.Dönni, H.Kitazawa, P.Fischer, F.Fauth, Journal of Alloys and Compounds, 289 (1996) 11.

[23] Ch.D.Routsi, J.K.Yakinthos, E.Gamari-Seale, Journal of Magnetism and Magnetic Materials, 110 (1992) 317.

[24] A.Szytuła, B.Penc, M.Kolenda, J.Leciewicz, N.Stüsser, A.Zygmunt, Journal of Magnetism and Magnetic Materials, 153 (1996) 273.

[25] B.Gibson, R.Pöttgen, R.K.Kremer, A.Simon, K.R.A.Ziebeck, Journal of Alloys and Compounds, 239 (1996) 34.

[26] E.Morosan, S.L.Buïko, P.C.Canfield, M.S.Torikachvili, A.H.Lacerda, Journal of Magnetism and Magnetic Materials, 277 (2004) 298.

[27] K.C.Watson, J.Crangle, K.U.Neumann, K.R.A.Ziebeck, Journal of Magnetism and Magnetic Materials, 140-144 (1995) 883.

[28] F.Hulliger, Journal of Alloys and Compounds, 218 (1995) 44.

[29] H.Fujii, M.Nagasawa, H.Kawanaka, T.Inoue, T.Takabatake, Physica B, 165&166 (1990) 435.

[30] H.Kitazawa, A.Matsushita, T.Matsumoto, T.Suzuki, Physica B, 199&200 (1994) 28.

[31] L.Keller, A.Dönni, H.Kitazawa, B.van den Brandt, Applied Physics A, 74 (2002) S686.

[32] S.Akamaru, Y.Isikawa, T.Kuwai, T.Mizushima, J.Sakurai, Y.Uwatoko, Physica B, 312-313 (2002) 466.

[33] S.Hane, T.Goto, T.Abe, Y.Isikawa, Physica B, 281-282 (2000) 391.

[34] J.Diehl, H.Davideit, S.Klimm, U.Tegel, C.Geibel, F.Steglich, S.Horn, Physica B, 206&207 (1995) 344.

[35] C.Schank, G.Olesch, J.Köhler, U.Tegel, U.Klinger, J.Diehl, S.Klimm, G.Sparn, S.Horn, C.Geibel, F.Steglich, Journal of Magnetism and Magnetic Materials, 140-144 (1995) 1237.

[36] T.Fujita, K.Satoh, Y.Maeno, Y.Uwatoko, H.Fujii, Journal of Magnetism and Magnetic Materials, 76&77 (1988) 133.

[37] H.Fujii, T.Inoue, Y.Andoh, T.Takabatake, K.Satoh, Y.Maeno, T.Fujita, J.Sakurai, Y.Yamaguchi, Physical Review B, 39 (1989) 6840.

[38] B.J.Korte, V.K.Pecharsky, K.A.Gschneidner, Journal of Applied Physics, 84 (1998) 5677.

[39] N.K.Singh, K.G.Suresh, R.Nirmala, A.K.Nigam, S.K.Malik, Journal of Applied Physics, 99 (2006).

[40] N.K.Singh, K.G.Suresh, R.Nirmala, A.K.Nigam, S.K.Malik, Journal of Magnetism and Magnetic Materials, 302 (2006) 302.

[41] A.E.Dwight, M.H.Muller, R.A.Conner Jr., J.W.Downey, H.Knott, Trans. Met. Soc. AIME, 242 (1968) 2075.

[42] H.Oesterreicher, J. Less-Common Metals, 30 (1973) 225.

[43] N.C.Tuan, V.Sechovský, M.Diviš, P.Svoboda, H.Nakotte, F.R.de Boer, N.H.Kim-Ngan, Journal of Applied Physics, 73 (1993) 5677.

[44] G.Ehlers, H.Maletta, Zeitschrift für Physik B, 101 (1996) 317.

[45] P.Javorský, P.Burlet, V.Sechovský, R.R.Arons, E.Ressouche, G.Lapertot, Physica B, 234-236 (1997) 665.

[46] P.Javorský, V.Sechovský, R.R.Arons, P.Burlet, E.Ressouche, P.Svoboda, G.Lapertot, Journal of Magnetism and Magnetic Materials, 164 (1996) 183.

[47] G.Ehlers, C.Geibel, F.Steglich, H.Maletta, Zeitschrift für Physik A, 104 (1997) 393.

[48] P.Javorský, L.Havela, V.Sechovský, H.Michor, K.Jurek, Journal of Alloys and Compounds, 264 (1998) 38.

[49] R.P.C.M.Gubbens, R.v.G., K.H.J.Buschow, Journal of Magnetism and Magnetic Materials, 177-181 (1998) 1149.

[50] P.Javorský, P.C.M.Gubbens, A.M.Mulders, K.Prokeš, N.Stüsser, T.J.Gortenmulder, R.W.A Hendrikx, Journal of Magnetism and Magnetic Materials, 251 (2002) 123.

[51] P.Javorský, V.Sechovský, L.Havela, H.Michor, Journal of Magnetism and Magnetic Materials, 177-181 (1998) 1052.

[52] G.Ehlers, H.Maletta, Zeitschrift für Physik B, 99 (1996) 145.

[53] G.Ehlers, C.Ritter, A.Kurtjakow, W.Miekeley, N.Stüsser, Th.Zeiske, H.Maletta, Physical Review B, 59 (1999) 8821.

[54] P.Javorský, P.Burlet, E.Ressouche, V.Sechovský, H.Michor, G.Lapertot, Physica B, 225 (1996) 230.

[55] J.Prchal, P.Javorský, V.Sechovský, M.Dopita, O.Isnard, K.Jurek, Journal of Magnetism and Magnetic Materials, 283 (2004) 34.

[56] V.Hulinský, K.Jurek, Zkoumání látek elektronovým svazkem, SNTL, Prague, 1983.

[57] KEVEX Manual, 1980.

[58] Yu.B.Kuz'ma, T.V.Pan'kiv, Russian Metallurgy, (1989) 208.

[59] PPMS Manual, Quantum Design, 2000.

[60] D.Schmitt, B.Ouladdiaf, Journal of Applied Crystallography, 31 (1998) 620.

[61] P.Wolfers, Journal of Applied Crystallography, 23 (1990) 554.

[62] G.Ehlers, Frustrierte magnetische 4*f*-Momente in intermetallischen Verbindungen der Lanthaniden, die in der ZrNiAl-Struktur kristallisieren; doctoral thesis, Berlin, 1997.

[63] F.Merlo, S.Cirafici, F.Canepa, Journal of Alloys and Compounds, 266 (1998) 22.

[64] J.Jarosz, E.Talik, T.Mydlarz, J.Kusz, H.Böhm, A.Winiarski, Journal of Magnetism and Magnetic Materials, 208 (2000) 169.

[65] E.Talik, M.Skutecka, J.Kusz, H.Böhm, J.Jarosz, T.Mydlarz, A.Winiarski, Journal of Alloys and Compounds, 325 (2001) 42.

[66] J.Kusz, H.Böhm, E.Talik, M.Skutecka, J.Deniszczyk, Journal of Alloys and Compounds, 348 (2002) 65.

[67] P.Javorský, P.Burlet, V.Sechovský, A.V.Andreev, J.Brown, P.Svoboda, Journal of Magnetism and Magnetic Materials, 166 (1997) 133.

[68] A.Szytu³a, B.Penc, E.Ressouche, Journal of Alloys and Compounds, 244 (1996) 94.

[69] A.V.Andreev, N.V.Mushnikkov, T.Goto, J.Prchal, Physica B, 346-347 (2004) 201.

[70] G.Asti, F.Bolzoni, Journal of Magnetism and Magnetic Materials, 20 (1980) 29.

[71] P.Javorský, M.Diviš, H.Sugawara, H.Sato, H.Mutka, Physical Review B, 65 (2002) 014404.

[72] P.Javorský, P.Daniel, E.Šantavá, J.Prchal, Journal of Magnetism and Magnetic Materials, in press (2006).

[73] P.Javorský, H.Sugawara, D.Rafaja, F.Bourdarot, H.Sato, Journal of Alloys and Compounds, 323-324 (2001) 472.

[74] S.Daniš, P.Javorský, D.Rafaja, Journal of Alloys and Compounds, 345 (2002) 10.

[75] M.Míšek, Nové supravodivé materiály v R(Ni,Cu)Al systému; bachelor thesis, Prague, 2006.

[76] H.Kitazawa, S.Eguchi, G.Kido, Physica B, 329-333 (2003) 1053.

[77] O.Garlea, E.Morosan, S.L.Bud'ko, J.L.Zarestky, P.C.Canfield, C.Stassis, Journal of Applied Physics, 95 (2004) 6921.

[78] D.X.Li, T.Yamamura, S.Nimori, K.Koyama, Y.Shiokawa, Journal of Alloys and Compounds, 418 (2006) 151.

[79] S.Baran, L.Gondek, J.Hernandez-Velasco, D.Koluorowski, A.Szytu³a, Journal of Magnetism and Magnetic Materials, 300 (2006) 484.

[80] E.Morosan, S.L.Bud'ko, P.C.Canfield, Physical Review B, 71 (2005).

[81] L.Gondek, S.Baran, A.Szytula, D.Kaczorowski, J.Hernandez-Velasco, Journal of Magnetism and Magnetic Materials, 285 (2005) 272.

[82] W.Bazela, L.Gondek, B.Penc, A.Szytula, N.Stusser, A.Zygmunt, Acta Physica Polonica B, 32 (2001) 3387.

Results in this thesis were subject of following publications:

$ErNi_{1-x}Cu_xAl$ series:

- J. Prchal, P. Javorský, O. Isnard, V. Sechovský, ***Neutron-diffraction study of the $ErNi_{1-x}Cu_xAl$ series**, Physica B*, **350**, Issue 1-3, Suppl. 1, 2004, e159-e161.
- J. Prchal, P. Javorský, V. Sechovský, M. Dopita, O. Isnard, K. Jurek, ***Development of magnetic order in the pseudo-ternary series $ErNi_{1-x}Cu_xAl$**, Journal of Magnetism and Magnetic Materials*, **283**, 2004, 34-45.

DyNiAl – single crystal:

- J. Prchal, A.V. Andreev, P. Javorský, F. Honda, K. Jurek, ***Bulk study of a DyNiAl single crystal***, *Journal of Magnetism and Magnetic Materials*, **272-276,** 2004, pp.e419-e420.
- A.V. Andreev, N.V. Mushnikov, T. Goto, J. Prchal, ***Magnetic anisotropy of a DyNiAl single crystal**, Physica B,* **346-347**, 2004, 201-205.
- J. Prchal, P. Javorský, K. Prokeš, B. Ouladdiaf, A.V. Andreev, ***Magnetic structures in DyNiAl single crystal***, *Physica B*, in press

$DyNi_{1-x}Cu_xAl$ series:

- J. Prchal, P. Javorský, S. Daniš, K. Jurek, J. Dlouhý, ***Structural study of the $DyNi_{1-x}Cu_xAl$ system***, *Czechoslovak Journal of Physics* **54**, 2004, suppl. D, 315-318.
- J. Prchal, P. Javorský, E. Šantavá, ***Evolution of magnetism in the $DyNi_{1-x}Cu_xAl$ series**, Physica B*, **359-361**, 2005, 220-222.
- J. Prchal, P. Javorský, B. Detlefs, S. Daniš, O. Isnard, ***Magnetic structures in $DyNi_{1-x}Cu_xAl$ pseudoternaries,** Journal of Magnetism and Magnetic Materials*, in press

R$Ni_{1-x}Cu_xAl$ pseudoternaries generally:

- J. Prchal, P. Javorský, M. Dopita, O. Isnard, V. Sechovský, ***Structure and magnetism in $RNi_{1-x}Cu_xAl$ (R = Er, Dy) compounds***, *Journal of Alloys and Compounds*, **408-412**, 2006, 155-157.
- J. Prchal, T. Naka, M. Míšek, O. Isnard, P. Javorský, ***Magnetic disorder in $RNi_{1-x}Cu_xAl$ compounds**, Journal of Magnetism and Magnetic Materials*, in press

concerning structural study:

- J. Prchal, H. Kitazawa, T. Furubayashi, P. Javorský, K. Koyama, V. Sechovský, ***Low-temperature structural study of the $TbPd_{1-x}Ni_xAl$ series***, *Physica B*, **378-380**, 2006, 1102-1104.
- J. Prchal, H. Kitazawa, O. Suzuki, ***Structural anomaly in the $Ce_{1-x}Y_xPdAl$ pseudo-ternary series***, *Journal of Alloys and Compounds*, in press